UNIVERSITAT ROVIRA I VIRGILI

DEEEA
Departament d'Enginyeria Electrònica, Elèctrica i Automàtica

Nanoelectronic and Photonic Systems Workshop

Tarragona, June 27-28, 2005

IEEE

Abstracts Book

Nanoelectronic and Photonic Systems Workshop

Tarragona, June 27-28, 2005

ISBN: 84-8424-023-1

Organising Comitee

Josep Pallares Marzal

Lluis F. Marsal Garvi

Josep Ferré Borrull

Anna Beltran Ras

Margarita Rebenaque Esteve

Schedule

Monday, 27th June

10:00 Plenary sesion 1

10:15 Coffee break

11:30 Plenary sesion 2

13:00 Lunch

14:45 Plenary sesion 3

16:00 Poster sesion

16:00 Coffee break

Tuesday, 28th June

10:00 Plenary sesion 4

11:00 Coffee break

11:30 Plenary sesion 5

13:00 Lunch

14:45 Plenary sesion 6

16:30 Best Poster Award

Invited Speakers

Plenary sesion 1

Development of sensors and transducers based on porous silicon

Prof. Hans Bohn

Institute of Thin Films and Interfaces, Division Bioelectric Signal Processes.
Research Centre Jülich, Germany

Plenary sesion 2

Aluminum anodizing and its application in micro- and nanoelectronics

Dr. Alexander Mozalev

Laboratory of Nanoelectronics, Belarussian.
State Univ. of Informatics and Radioelectronics, Minsk, Belarus

Plenary sesion 3

Ballistic effects in advanced MOSFET along the roadmap

Prof. Enrico Sangiorgio (Distinguished Lecturer IEEE)

Dipartimento di Elettronica, Informatica e Sistemistica.
Universitá di Bologna, Italy

Plenary sesion 4

Nonlinear Photonic Crystals: a Wealth of Novel Phenomena

Prof. Gaetano Assanto

Nonlinear Optics and Optoelectronics Lab., Dept. of Electronics
University "Roma Tre", Rome, Italy

Plenary sesion 5

Microcavities and Filters in Photonic Crystals

Prof. Min Qiu

Dept. of Microelectronics and Information.
Technology Royal Institute of Technology (KTH), Kista, Sweden

Plenary sesion 5

Tailoring and analysis of polymer surfaces

Prof. Jean Jacques Pireaux

Physics Department, Facultes Universitaires Notre-Dame de la Paix, Namur, Belgium

Index

Invited Conferences

Posters

Invited Conferences

Development of sensors and transducers based on porous silicon

Prof. Hans Bohn

Institute of Thin Films and Interfaces, Division Bioelectric Signal Processes
Research Centre Jülich, Germany

Abstract

Porous Silicon (PS) is a versatile and attractive material with all the advantages of silicon technology, namely miniaturization, integration of signal processing circuitry and low cost. The added advantage of its huge specific surface area of 3 – 300 m2/cm3 makes it a material of choice for may types of sensors like bio- and chemosensors. Its properties like pore morphology, porosity, layer thickness, etc. can be conveniently adjusted by selecting proper preparation parameters. Basically three types of sensors can be distinguished where PS comes into play: a) a PS structure comprises the sensing element b) PS is used as an sacrificial layer in the fabrication of a sensor and c) components made of PS (in particular optical) are built into a sensor. We will describe and discuss various types of sensors which incorporate these principles. Also some limitations will be considered which up to now prevent a large scale introduction into the market.

Ballistic effects in advanced MOSFET along the roadmap

Dr. E. Sangiorgio

Dipartimento di Elettronica, Informatica e Sistemistica
Universitá di Bologna, Italy

Abstract

The ITRS roadmap projects the introduction of MOSFETs with gate length LG down to 25 nm by the year 2007. The accurate modelling of these devices is a challenging objective, since both quantization and non-equilibrium transport effects have to be properly taken into account.
A tempting simplification consists in neglecting the scattering and developing ballistic transport models. However, the a-priori assumption of the negligible role of scattering is difficult to justify.
In this talk, a Monte-Carlo simulator including quantum corrections is used to demonstrate that, for gate length down to 14 nm, scattering still controls the ON current
(ION), which for LG = 25 nm is overestimated by about a factor of 1.5 in the ballistic model.
The impact of technology scaling on ballistic effects has been investigated by computing the ratio of the maximum current ION to its ballistic limit IBL for MOSFETs designed according to the 2003 Roadmap, down to the 45 nm node.
Our results show that in the case of devices for which phonon scattering is dominant the ratio ION/IBL exhibits an universal dependence on gate length for the considered technological nodes.

Nonlinear Photonic Crystals: a wealth of novel phenomena

G. Assanto

Nonlinear Optics and Optoelectronics Lab. Dept. of Electronics
University "Roma Tre", Italy

Abstract

Using a three-dimensional + time Finite Difference Time Domain code, various dispersive photonic crystal structures are investigated, including cubic and/or quadratic nonlinearities.
In particular, the density of states can be populated by way of four-wave mixing, optical parametric oscillations can take place in photonic crystals with isotropic media, a defect-resonance can be tuned by the level of excitation, an ultrafast power-tunable wavelength shifter ca be envisaged in a signal-seeded PC cavity. Finally, using parametric media, frequencies in the TeraHertz range can be generated via optical rectification, and virtual bandgaps excited by backward second harmonic generation.

Microcavities and filters in photonic crystals

Min Qiu

Department of Microelectronics and Information Technology
Royal Institute of Technology (KTH), Kista, Sweden

Abstract

Optical microcavities have attracted much attention due to their potential applications in many various photonic devices, while microcavities in photonic crystal slabs exhibit even more attractive properties such as high quality factor (Q) with ultra small modal volume.
This presentation will provide a review on our recent work on design of photonic crystal microcavities. The cavity modes are calculated using a combination of finite-difference time-domian techniques and Padé approximation with Baker's algorithm. The principle of obtaining high Q values will be discussed. Several recent designs of optical filter based on photonic crystal cavities will also be presented and discussed.

Tailoring and analysis of polymer surfaces

J.J. Pireaux

University of Namur
LISE Laboratory, Belgium

Abstract

Plasma processes can be used to clean, erode, roughen, activate a material's surface, or to deposit a thin/thick layer on top of a substrate. This presentation will be focused on the use of RF 13.56 MHz low pressure cold plasmas to modify polymer surfaces. Trough one example – the deposition of SiOx onto polypropylene – it will be shown that spectroscopic information allows to go beyond the use of (simple) recipes and to understand the reason of a good or bad adhesion. X-ray photoelectron spectroscopy is used to disclose the elemental and chemical composition of the (modified) material surface, contact angle measurement to evidence hydrophobicity change and to calculate surface energies, while infrared spectroscopy (in the multiple reflexion mode) complements the understanding of interfacial phenomena.

Abstracts

Anodizing of aluminium foils

L. Vojkuvka*, L.F. Marsal and J. Pallares

Rovira i Virgili University, ETSE-DEEEA

*Tel.: 977 55 87 64 - e-mail:lukas.vojkuvka@urv.net– http://www.urv.es

Abstract

Several experimental trials of aluminum anodization under specific conditions were carried out in this work. Samples were anodized at different voltages varying from 18 – 25 V for sulfuric acid and 40 – 60 V for oxalic acid. The eletropolishing pre-step was carried out in order to obtain a smooth mirror-finish surface of aluminum foils. In order to verify the results, the images of samples with the scanning electron microscopy were achieved.

1. Introduction

One of the relatively new and expanding branch in research area is nanotechnology. In this area is included the study and produce of Al_2O_3 nanostructures, a material with unique chemical and electrical properties. These Al_2O_3 structures have a comparatively low fabrication cost, and a wide range of applications in areas such as electronic, optical and semiconductor devices.

In the last few decades, plenty of experiments and investigations for obtaining porous anodic alumina were done in several research groups and organizations all over the world. During the observation, the phenomenon of self-organized pore growth was noticed and can be found in many technical reports and specialized publications [1-5]. This essential phenomenon of self-ordering leads to a densely packed pore structure that is achieved under specific conditions. Highly ordered hexagonal structures of pores occur in a small processing window, whereas non-ordered pore structures can be obtained from wide range of parameters [1].

2. Experimental part

High purity, 99,999% Al foils from the Goodfellow Cambridge Ltd. were used as the working samples. The specific pre-treatment steps such as an annealing and an electropolishing were done in order to obtain suitable material for the next step - anodization. Firstly, the foils were annealed in a nitrogen atmosphere at 400 ºC for 3 hours to remove mechanical stresses and recrystallize. Then, the process of electropolishing was done.

3. Electropolishing

Several experiments were carried out in order to obtain a smooth mirror-finish surface of aluminum foils. The following conditions were applied. The magnetic stirrer was used to avoid the impact of bubble foam on the final surface appearance. The electrolyte of ethanol and tetrachloric acid was prepared according to the procedures described above, was cooled down in the small double vessel to a temperature about 5 °C. Each of the samples of 1 cm² were cut away from the aluminum foil and placed in an anode sample window and fixed, to a plastic cover, by screws. An inox cathode together with an anode were put into the vessel using the frame with tongs. Consequently, the system was connected for several minutes under a constant voltage supply, i.e., a potenciostatic regime, ranging for each experiment from between 20 to 25 V.

Although the samples were anodized with voltages ranging from 20 up to 25 V and showed out quite similar results with polished mirror-finish surfaces, using the voltage of 20 V the one without any obviously observable spots and scratches was obtained (Fig. 1). The polishing runtime from 3 – 4 minutes was examined as sufficient.

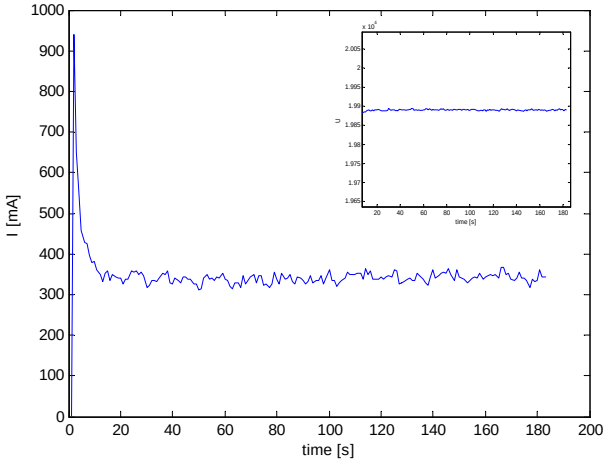

Fig.1. Current curve of electropolishing , constant voltage profile in the upper corner

4. The anodization of aluminium

The samples with a mirror-finished surface for the following anodization were prepared using the procedures of electropolishing examined previously. In resume, as electrolytes: 10% H_2SO_4 cooled to approximately 0 ºC and 0.3M $(COOH)_2$ with temperature of 20 ºC, an inox cathode and rigorous stirring were utilized. In all experiments the constant, i.e. potenciostatic, voltage within the range of 18 to 25 V or 40 – 60 V at different times were applied to the system.

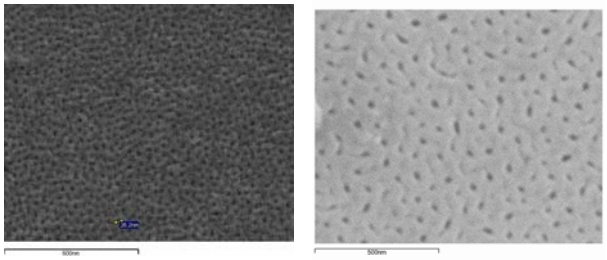

Fig.2. SEM images of porous alumina prepared in sulfuric (left) and oxalic (right) acid.

The difference between oxide structures prepared in sulfiric or oxalic acid can be seen in Fig.2.In both cases the porous stucture is not ordered and the pores grows randomly over the sample surface. The pore´s density is higher using sulfuric acid and the pore diameter is also smaller than that one from oxalic acid.

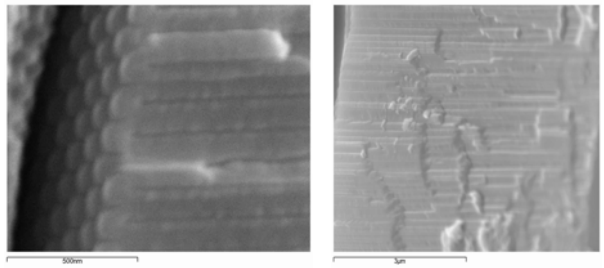

Fig.3. Cross-section of porous alumina.

The SEM cross-section image on the left of Fig.3. shows the bottom of the oxide layer. Notice, that pores at the bottom are arranged in hexagonal array. This confirms that the pattern of ordered dots is created in the aluminium substrate after the removal of oxide layer. Therefore, if the sample with such as pattern is anodized for second time using the same conditions as in the first step, the ordered porous structure can be expected. This process is called two step anodization and can show out interesting results in the future. The image on the left of Fig.3. illustrates the regularity of pores that are thin and straight. The pore diameter, ordered arrangement and porosity of structure are the main parameters that has to be controlled in the process of anodizing.

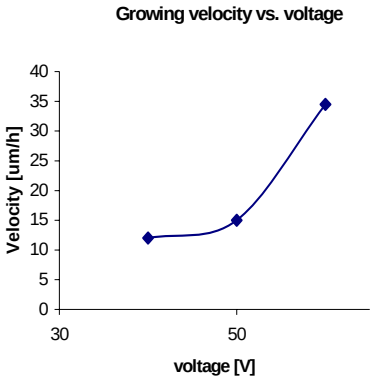

Fig.4. SEM images of porous alumina prepared in sulfuric (left) and oxalic (right) acid.

In the Fig.4., there is example of experimental analisis. The thickness of oxide layer was measured using the SEM cross-section images. Later, knowing the time, the approximate velocity of oxide growing was calculated. As can be seen, the thickness of oxide has a strong dependence on the applied voltage. The voltage is just one of the various parameters influencing the process. These parameters has to be studied and examined in detail.

5. Conclusions

The process of anodization was examined in detail. The alumina porous structructure was created after several experimental trials. The electropolishing pre-step was analysed and new methods and techniques were proposed. The sample examination with scanning electron microscopy (SEM) was done and several analysis and images were obtained.

References

[1] O. Jessensky, F.M., and U. Gösele, *Self-organized formation of hexagonal pore arrays in anodic alumina.* Applied Physics Letters, 1998. **72**(10): p. 1173-1175.

[2] Li, A.-P., Müller, F., Birner, A., Nielsch, K. and Gösele, U., *Polycrystalline nanopore arrays with hexagonal ordering on aluminum.* Journal of Vacuum Science & Technology, 1999. **A 17**(4 Part 1): p. 1428-1431.

[3] A. P. Li, F.M., A. Birner, K. Nielsch, and U. Gösele, *Hexagonal pore arrays with a 50–420 nm interpore distance formed by self-organization in anodic alumina.* Journal of Applied Physics, 1998. **84**(11): p. 6023-6026.

[4] Das, B., *Investigation of Nanoporous Thin-Film Alumina Templates.* Journal of The Electrochemical Society, 2004. **151**(6): p. 46-50.

[5] Hennesthal, C., Anodization of aluminum: New applications for a common technology. 2003, JPK Instruments AG.

Discrimination between Chronic Obstructive Pulmonary Disease (COPD) individuals and healthy people using their exhaled breath SPME-GC-MS profiles

M. Vinaixa, J. Brezmes, E. Llobet, X. Vilanova, X. Correig

Departament d'Enginyeria Electrònica, Elèctrica i Automàtica, ETSE, Universitat Rovira i Virgili, Avda. Països Catalans, 26, 43007 Tarragona maria.vinaixa@urv.net

Abstract

This paper proposes a new method for COPD diagnosis. The method is based on the multivariate chromatographic comparison of exhaled breath. Patients could benefit from the application of this technique due to its non invasive nature. Moreover the method could report valuable chemical information at early development stages of the disease.

1. Introduction

COPD is a disease state characterised by an airflow limitation that is not fully reversible. Spirometric evaluation should be used to confirm the diagnosis when suspicious symptomatology is present. Chronic cough and sputum production have a variable relationship to airflow limitation. The epidemiological and pathological disease manifestations have a statistically significant, but not a high degree of correlation with COPD confirmed patients by physiological testing. Variability in clinical patterns is common in COPD and thus makes diagnosis difficult. Non-invasive sampling and chemical analysis of breath gases could provide valuable information related to health. Breath gases are indicators of metabolic end-products and therefore VOC's present in expired breath may give information about lung metabolic conditions. Many studies on breath analysis by GC-MS have been reported so far. In these papers several hundreds of different compounds in human breath have been reported. Nonetheless, these studies have not led to any practical diagnostic method due to the overwhelming complexity of the analysis carried out by GC-MS [1]. The goal of this paper is to discriminate between healthy and COPD diagnosed individuals comparing their exhaled breath GC-MS profiles in a fast and easy way.

2. Material and methods

The exhaled breath air from volunteers was collected in a 500 mL Tedlar bag. The bag was subsequently sampled through a septum port with a 75-µm CAR/PDMS SPME fiber at room temperature for 20 minutes. Chromatographic profiles were obtained desorbing volatiles trapped on the fibre in the injector port of a Shimadzu QP5000 GC/MS equipped with a Supelcowax (30m x 0.25mm x 0.25µm ID) capillary column purchased from Supelco (Bellafonte, PA) at 280ºC. The GC oven was held at 40ºC during 1.5 minutes, after which the oven was programmed to increase its temperature to a final value of 250ºC at a 10ºC/min rate. Helium was the carrier gas with a flow rate of 1.0 mL/min . Mass spectrometry analysis was carried out in the electron impact ionization mode (70 eV) with a scan range of 35 to 220 amu. The ion source temperature was kept at 250ºC.

3. Experimental

For the first experiment a total of 6 healthy volunteers were considered. They belonged to 3 different groups according to their smoking habits. Each volunteer was sampled twice. Three different SPME-extractions were performed for each sampling bag as it is shown in Table 1.

	Individuals	Sampling Bags	Experimental points
Smokers	Subject 1	2	6
	Subject 2	2	6
Ex-Smokers	Subject 3	2	6
	Subject 4	2	6
Non-Smokers	Subject 5	2	6
	Subject 6	2	6

Table 1. Measurements performed on experiment 1

In the second experiment, as it is shown in Table 2, a total of 4 ill volunteers were analysed. Two of them were diagnosed as Mild COPD and two of them as Severe COPD

	Individuals	Sampling Bags	Experimental points
Severe COPD	Subject 7	1	3
	Subject 8	1	3
Mild COPD	Subject 9	1	3
	Subject 10	1	3

Table 2. Measurements performed under experiment 2

Experiment 3 was dedicated to study the ability of the method to distinguish between healthy and COPD

diagnosed individuals. The first three replicates for each individual of experiment 1 along with measurements of experiment 2 were considered. In the healthy group, smokers and non-smokers were included in the model to study the influence of smoker habits on predictions made by the model.

4. Data treatment

All chromatographic profiles obtained were pre-processed before pattern recognition analysis was applied. Raw mass spectrometry files (in text format) were imported by a written-in-house lab-view based software in to MATLAB for further multivariate processing. A first step consisted on reducing noise levels for every m/z channel, so that the overall background noise was lowered. The minimum response value for each m/z channel was subtracted from all other response values in the same channel. Another important step for comparing chromatograms by multivariate modelling was to align the chromatograms derived from each sample. Although GC/MS analysis is considered to be very reproducible under optimized injection and GC conditions, some differences in retention times between different injections will always occur. Such differences may arise from small variations in gas flow, solvent composition, temperature, or other unknown factors that influence retention time reproducibility. Chromatograms were aligned finding the maximal covariance between the data. Matrix data response was generated considering each measurement in rows and the TIC value gathered in each scan as columns. This matrix was used to attempt a fuzzy ARTMAP-based classification of the samples according to the goal defined in each experiment. A previous PCA variable reduction process was performed to the data matrix and the scores on the first 10 PCs were retained for further processing and were used as input variables to the neural net classifier.

5. Results and discussion

In experiment 1 a cross validated Fuzzy Artmap classifier with a previous PCA variable reduction achieved 83% success rate trying to discriminate among the three groups defined (smokers, non-smokers and ex-smokers) . The main part of variance in this model is used to explain the difference between smokers and non-smokers. This analysis revealed that being a smoker acquired a high level specific weight in the mathematical model. Misclassifications are always produced between the non-smokers and the ex-smokers group. Figure 1 shows a PCA score plot from experiment 2. As it can bee seen the method is able to clearly distinguish between the two types of COPD by the comparison of chromatographic profiles. From this projection it can be derived that different severity COPD states produce different volatile pattern profiles that allow their discrimination. The fuzzy Artmap classifier achieved 100% of success rate trying to distinguish among the two different states of this disease. Figure 3 reveals the ability of the model to predict whether it can distinguish between healthy and COPD diagnosed volunteers. Distinction is produced along the second principal component that only explained a 13% of the total variance. The first principal component is dedicated mainly to distinguish between smokers and ex or non-smokers groups. Cross-validated PCA-Fuzzy Artmap success rate fell down to 73% trying to distinguish between three groups: healthy, moderate COPD and severe COPD.

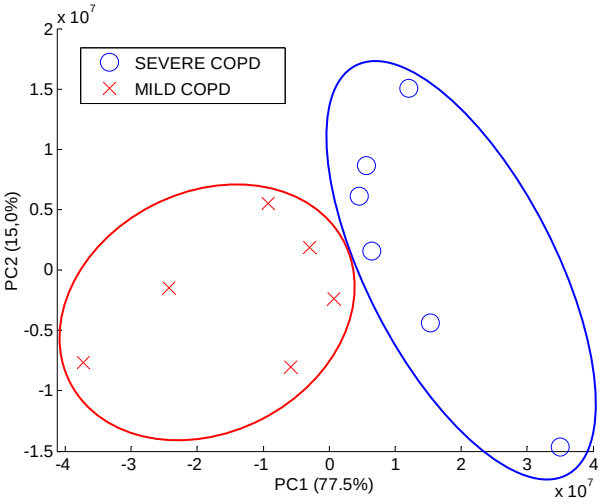

Fig.1 2D-PCA scores plot from experiment 2

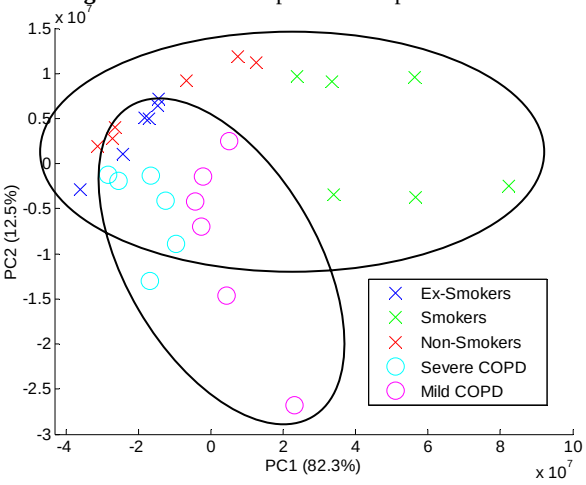

Fig.2 2D-PCA scores plot from exp 3. Tendency distinction between healthy and ill individuals is showed along PC2

6. Summary and conclusions

A new method for COPD diagnosis has been proposed. It is advantageous over other related methods since it is based in exhaled breath and therefore is a non invasive technique. The methodology under study is in a preliminary stage. The sampling mechanism device must be improved since some artefacts have been detected. Inherent volunteers related effects as diet, smoke conditions or style of life greatly affect the mathematical model. Inherent volunteers related effects as diet, smoke habits or style of life could greatly affect the mathematical model. Healthy and ill classification of individuals could remain masked under some of these effects diminishing the ability of model prediction.

References

[1] C. Di Natale, E.Martinelli, Lung cancer identification by the analysis of breath by means of an array of non-selective gas sensors, Biosensors and Bioelectronics 18 (2003)

Photonic Band Gaps in Metallo-Dielectric Photonic Crystals with Real Metals into a Porous Silicon Matrix

M. A. Ustyantsev, L. F. Marsal, J. Ferré-Borrull, and J.Pallarès

Departament d'Enginyeria Electrònica, Elèctrica i Automàtica, ETSE, Campus Sescelades, Universitat Rovira i Virgili, Avda. Països Catalans 26, 43007 Tarragona, Spain
Tel: +34977559625, Fax: +34977559605, e-mail: lluis.marsal@urv.net

Abstract

We studied, by using a modified plane-wave method and the transfer-matrix method, the band gap properties of two-dimensional metallodielectric photonic crystals with square and triangular lattices of circular rods embedded into a silicon matrix. The existence of absolute photonic band gaps in the TM polarization and the dependence of their width as a function of the radius has been investigated. The results show the possibility of achieving a relative band gap width larger than 10% for filling fractions away from the close packed condition for both lattices. The effect of considering real values for the optical parameters of the metals has been also studied.

1. Introduction

In recent years there has been a growing effort devoted to the study of two-dimensional metallodielectric photonic crystals (MDPCs) [1-4] as the inclusion of metallic components can enlarge the size of the gaps [5, 6]. From a practical point of view, metallic photonic crystals can be realized by electrochemical deposition of a metal into the holes of a periodic structure of air holes in a dielectric [7, 8].

In this work we investigate MDPCs with square and triangular lattices of circular rods in a Si matrix. Only TM-polarization is considered, since TE polarization exhibits more complex behavior due to the presence of surface plasmon polaritons. The metallic features will be modeled by a Drude dispersion relation. In section 2 we investigate the width of the band gaps as a function of the filling fraction. In this section dissipation of the metal is not considered, since, as shown in [2], the photonic band structures are only slightly perturbed for moderate dissipation levels. Then, in section 3, we study the differences in the band gap width that arise for different real metal components.

2. Photonic Band Gap width in Si-Matrix MDPCs

For this section, the modified plane wave method (PWM)[2] was generalized in order to take into account background materials different from air. The number of plane waves used in the expansion of the electromagnetic fields was 225, and the maximum difference in the band structures is less than 1% for the ten lowest bands.

In all of our calculations the photonic crystal is composed of circular metallic rods with radius r in the square and triangular lattices with lattice constant a. The dielectric constant of the rods is of Drude type: $\varepsilon(\omega)=1-\omega_p^2 / \omega(\omega+i\gamma)$, with the plasma frequency ω_p chosen such that $\omega_p a/2\pi c = 1.0$, where c is the speed of light. The dissipation constant γ is taken to be 0. The background dielectric constant ε_b was 12 (as an approximate value for silicon) and was frequency-independent.

Figure 1 shows the photonic band structure for a square lattice of circular metallic rods. There are three band gaps – the large one between the zero frequency and the cutoff frequency defined by the first band (TM0-1), a smaller one between the first and the second bands (TM1-2) and the new one between the third and forth bands (TM3-4). This last one is new since it was absent in the case of MDPC with air background.

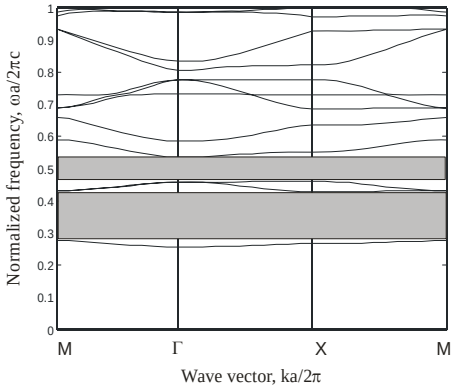

Fig.1. Photonic band structure for a square lattice of metallic rods with r/a=0.472. Shaded areas are the photonic band gaps.

The dependence of the relative band gap width ($\Delta\omega/\omega_g$) with the r/a ratio is plotted in Figure 2. It can be observed that the TM1-2 PBG appears for a filling factor above 0.19 and is monotonically increasing until

the close packed condition is reached. The $\Delta\omega/\omega_g$ of the new TM3-4 gap has the same behaviour except that it appears for larger filling factors.

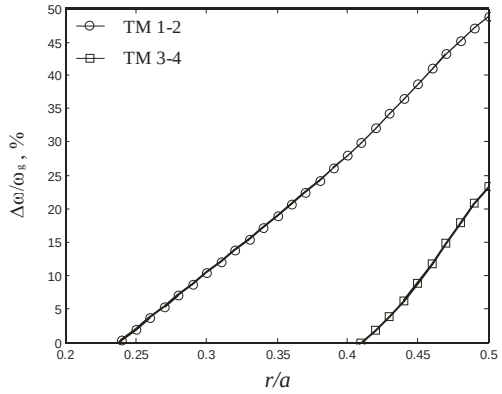

Fig.2. Relative size of the band gaps as a function of r/a for a square lattice of circular metallic rods in Si.

In the case of a triangular lattice, there are two band gaps: a large one below the cutoff frequency defined by the first band (TM0-1) and a second one between the second and third bands (TM2-3). It is important to note that this second band gap does not exist in the case of air background. The $\Delta\omega/\omega_g$ dependence for triangular lattice is plotted in Figure 3. It can be observed that TM2-3 PBG does not appear for filling factors less than 0.52 and that in this case the $\Delta\omega/\omega_g$ is also monotonically increasing with r.

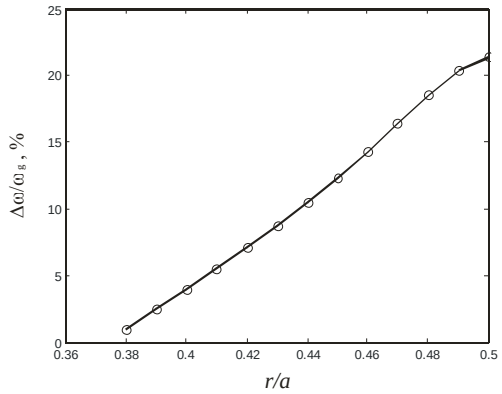

Fig.3. Relative size of the band gap as a function of r/a for triangular lattice for circular metallic rods in Si.

3. Reflectance Spectra for Real Metallic Components

The results presented in the previous section correspond to a metal with a hypothetic plasma frequency matched to the lattice constant of the Si matrix. However, if Macroporous Silicon Photonic Crystals made by electrochemical etching are used as matrices for MDPCs there exist some constraints to the lattice constants and pore sizes an the plasma frequency of real metals are also limited. In this section we study the influence of using different metals in the MDPC. Figure 4 shows the reflectance spectra for light propagating in the ΓM direction of the photonic crystal for three different constituent metals, Ag (ω_P=7.2eV, γ=0.05eV), Al (ω_P=15eV, γ=0.05eV) and Ti (ω_P=14.8eV, γ=1.4eV). The reflectance spectra have been calculated with the Transfer-Matrix Method (TMM)[9] for a square lattice with lattice constant 1μm and with the dissipation included in the Drude model. The spectra show that the positions of the PBGs and their width vary slightly with the inclusion of the real values for ω_P and γ. The main difference is the level of reflectance which is affected by the absorption produced by the dissipation.

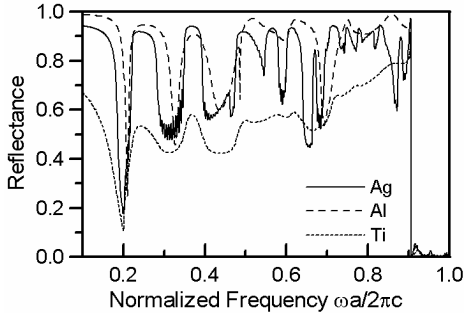

Fig.4. Reflectance spectra in the ΓM direction for MDPCs with three different metallic components.

4. Conclusions

We have shown that 2D Metallo-dielectric photonic crystals consisting of square or triangular lattices of circular rods embedded into a silicon matrix can be used for photonic band gap engineering because the width of the band gaps can be tuned with the filling fraction. Furthermore, for square lattices we observed that a new photonic band gap (not existing for air background) opens and that this gap can reach a gap to midgap frequency ratio bigger than 20% for filling fractions below the close packed condition. In the case of a triangular lattice a new gap also appears which can reach a gap to midgap ratio bigger than 15%. We have also investigated the effect of using values of plasma frequency and dissipation for the Drude model corresponding to real metals. We have seen that the inclusion of such parameters does not vary substantially the positions and width of the gaps, while the absorption is greatly influenced.

References

[1] A. Moroz, *Phys. Rev. Lett.* 83, 5274, 1999.

[2] V. Kuzmiak, A.A. Maradudin, and F. Pincemin, *Phys. Rev. B.* 50, 16835, 1994.

[3] K. Sakoda, et al., *Phys. Rev. B*, 64, 045116, 2001.

[4] O. Takayama and M. Cada, *Appl. Phys. Lett*. 85, 1311 , 2004.

[5] Xiangdong Zhang and Zhao-Qing Zhang, *Phys. Rev. B.* 61, 9847, 2000.

[6] A. Moroz, *Phys. Rev. B.* 66, 115109, 2002.

[7] J. Choi, G. Sauer, K. Nielsch, R.B. Wehrspohn, and U. Gösele, *Chem. Mater*. 15, 776, 2003.

[8] K. Nielsch, R.B. Wehrspohn, S.F. Fischer, H. Kronmüller, J. Barthel, J. Kirschner, T. Schweinboeck, D. Weiss, and U. Gösele, *MRS Symp. Proc.* 705, Y9.3.1 ,2002.

[9] J. B. Pendry and A. MacKinnon, Phys. Rev. Lett. 69, p. 2772, 1992.

Features of WO_3 Thin Films Deposited with Interruptions

S. Vallejos, V. Khatko and X. Correig

Dept. d'Enginyeria Electrònica, Elèctrica i Automàtica, Universitat Rovira i Virgili, Avda. Països Catalans 26, 43007, Tarragona, España, stella.vallejos@urv.net

Abstract

WO_3 thin films were deposited by reactive r.f. sputtering from a pure tungsten target. Four types of films were prepared, one of them without interruptions and the others with three interruptions during sputtering process. Time of interruptions was different for each sample: 30s, 90 s and 300 s. Morphology and structural properties have been study. It was found that monoclinic phase with *Pc* symmetry is presented in the metal oxide films and grain size decreases with the interruption time. On the base of these films, sensing layers were prepared and their response to NO_2 was investigated. The thin films with the interruption time more than 90 s showed the best sensing properties.

1. Introduction

Grain size reduction in metal oxide films is one of the key factors to enhance the gas sensing properties of semiconductor layers. A way to create metal-oxide thin films with small grain size is to use a special regime of thin film deposition by the dc magnetron, ion-beam or r.f. sputtering of pure metal or metal oxide targets. This regime implies the deposition of the thin film with one or several interruptions during the deposition process. In this case "extra" interfaces are introduced into a thin film body. During the interruption of the deposition process, an equilibrium surface could be formed due to the free surface bond saturation by the atoms from residual atmosphere and/or the structural relaxation of the interface. Early, it was found that the total thickness of the WO_3 films decreased with the number of interruptions [1, 2]. The aim of this paper is to show the influence of interruptions time on the morphology, and gas sensing properties of the WO_3 films deposited. Moreover, the structural properties of the films with and without interruptions are presented.

2. Experimental

WO_3 thin films were deposited on top of silicon wafers, oxidized in dry air, by reactive r.f. magnetron sputtering – ESMS100 Edwards sputtering system – of pure tungsten target of 99.95%. The sputtering atmosphere consisted of Ar-O_2 mixed gas and its flow rate was controlled by separate gas flowmeters to provide an Ar : O_2 flow ratio of 1 : 1. The deposition chamber was maintained at 5×10^{-3} mbar during sputtering. The r.f. sputtering power was 100 W. Thin films of WO_3 with zero and three interruptions during the deposition process were prepared. Three interruption times were applied: 30s, 90s and 300s. The deposition time was up to 40 min for all thin films. Morphology of the WO_3 thin films was determined by atomic force microscopy (AFM) – Multimode Scanning Probe Microscope. The estimation of grain size was realized using Nanoscope software. A phase composition of the sensing layers was determined by X-ray diffraction (XRD) – Siemens D5000 diffractometer – operated at 40 kV and 30 mA with CuKα radiation.

The top contacts to the sensing layers were formed using air dry silver paste – Heraeus AD1688-06 – and annealing at 400°C during 2 h for the contact formation. Using this paste, the test samples were fixed on a ceramic heater prepared according to the method reported in [3]. The response of the films to nitrogen dioxide was investigated. The sensors were kept in a temperature and moisture controlled test chamber. The sensors were operated at 250ºC. The resistance of the sensing layers in the presence of either pure air (R_{air}) or the pollutant (R_{gas}) at the different concentrations was monitored and stored in a PC.

3. Results and Discussion

3.1. Film morphology

Figure 1 shows the surface morphology and roughness profile of the WO_3 films investigated by AFM. Mean diameter of grain size calculated from these image are presented in Table 1. These results clearly point out the influence of the interruption time of the sputtering process on the morphology of deposited metal oxide films. It can be seen that increasing the interruption time leads to a decrease in the grain size on the film surface. On the other hand, the roughness profile analysis along the horizontal lines of the AFM pictures shows that the sample deposited with the interruption time up to 300 s is smoother than the one deposited with the interruption

time up to 30 s.

Interruption time, s	0	30	90	300
Grain size, nm	24	22	20	17

Table 1. Mean grain size on the film surface as a function of the interruption time

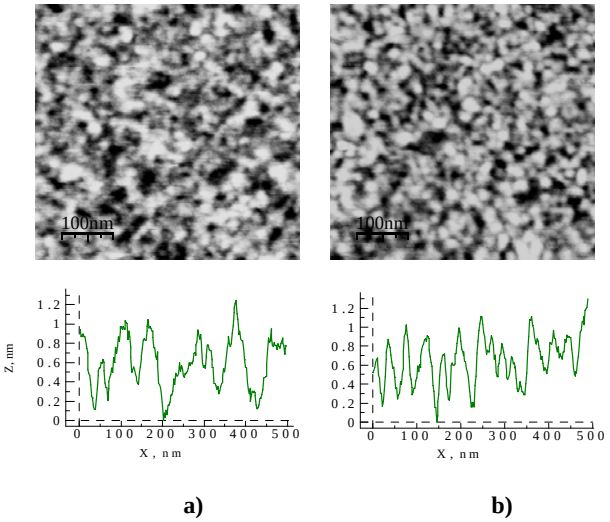

Fig.1. AFM surface morphology and roughness profile of WO_3 thin films with interruption time up to 30 s (a) and 300 s (b)

3.2. Structural features

XRD data shows that WO_3 thin films as deposited have amorphous structure. After annealing at the temperature from 400ºC to 800ºC, stable monoclinic phase with *Pc* symmetry (ICDD card no. 872386) is presented. The cell parameters are a=5.277Å, b=5.156Å, c=7.666Å, β=91.742º.

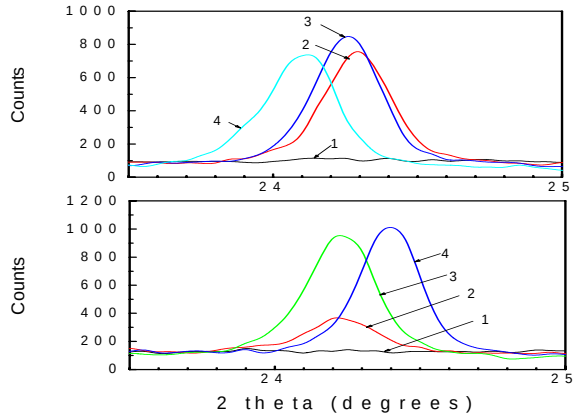

Fig.2. XRD spectra of WO_3 films deposited without interruptions (top) and with three interruptions (bottom).

1 - 300ºC, 2 - 400ºC, 3 - 500ºC, 4 - room temperature after annealing at 800ºC.

3.3. Gas sensitivity studies

The responses of the films with the interruption time up to 30 s, 90s and 300 s to nitrogen dioxide were analyzed at operating temperature of 250°C. Figure 3 shows the response of the tungsten oxide layers to NO_2. Sensitivity to NO_2 for these sensors was calculated using the relation $S = (R_{gas}-R_{air})/R_{air}$ and is presented in Table 2.

Interruption time, s	30	90	300
1 ppm	0.78	0.85	0.86
2 ppm	1.47	1.74	1.8

Table 2. Sensor sensitivity (S) in the presence of 1 ppm and 2 ppm of NO_2 as a function of the interruption time (at 250 °C)

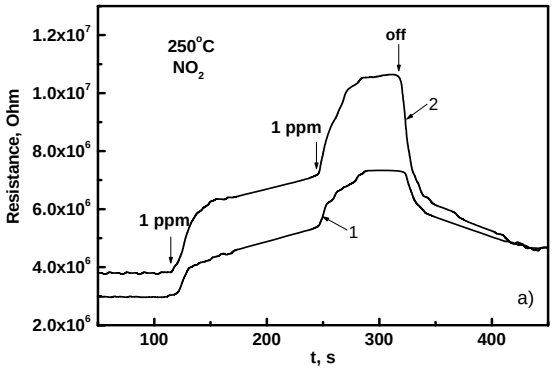

Fig.3. Response of the WO_3 thin films with interruption time up to 30 s and 300 s to NO_2 at 250°C.

4. Conclusions

Morphological, structural and sensing properties of the tungsten oxide thin films deposited without and with three interruptions have been studied. It was shown the influence of the interruption time on morphology and sensing properties of WO_3 sensing layers. Increasing interruption time produced a decrease of the grain size. WO_3 films crystallize a monoclinic phase which is stable in a range from 400ºC to 800ºC. Layers with the interruption time more than 90 s show better sensitivity.

References

[1] V. Khatko, J. Calderer, E. Llobet, and X. Correig, *Sens. Actuators B, Chem*, in press, 2005.

[2] V. Khatko, J. Calderer, E. Llobet, and X. Correig, presented at Proceedings of the European Materials Conference E-MRS 2004 FALL MEETING, Warsaw (Poland), 2004.

[3] J. Hubálek, K. Malysz, J. Prá ek, X. Vilanova, P. Ivanov, E. Llobet, J. Brezmes, X. Correig, and Z. Sv rák, *Sens. Actuators, B*, vol. 101, pp. 277-283, 2004.

THICK FILM TITANIA BASED SENSORS FOR DETECTION OF OXYGEN AT PPM LEVELS

E. Sotter*, X. Vilanova, A. Vasiliev, X. Correig
Department of Electronic Engineering, University Rovira i Virgili
Av. Països Catalans 26, 43007 Tarragona, Spain
*esotter@urv.net

Abstract: The development of pure titania and Nb-doped titania based sensor is reported. Active materials were synthesized via sol-gel and calcined at temperatures between 600ºC – 900ºC. Samples which contained mainly anatase phase were selected and deposited over alumina substrates through thick film technique. Sensors were tested to traces of O_2 in N_2 balance, at working temperatures of 400ºC and 500ºC.
Keywords: oxygen sensor, titania, thick film.

INTRODUCTION

Due to many advantages as low cost, small size and robustness, semiconductors sensors appear as a good solution for oxygen detection. In some industrial processes levels of oxygen must be detected and controlled in ppm scale [1]. Although some authors had reported detection of oxygen at ppm levels [2, 3], most of them were made through thin film technology. For industrial applications the most usual technology is thick film [2], because it is easier to fabricate and to dope than thin film sensors [4]. For thick film sensors, detection of traces of oxygen is still a very difficult goal to reach, usually need high temperatures (700 ºC<). Detection at 400 ºC was reported for Sharma et al. [5] butt detection limit was around 1200 ppm.

In this communication we report on the detection of oxygen at levels between 1ppm to 20 ppm using a thick film sensor working at 400 ºC-500 ºC. As active material it was employed titanium dioxide, which is widely used for oxygen detection in semiconductor gas sensors [6]. To increase oxygen sensitivity and decrease the resistivity of the active layer, titania was doped with Nb^{+5} in a concentration of 3 at% [7, 8]. It was also reported that Nb^{+5} help to maintain the anatase phase of titania until 700 ºC, which permit that detection reaction take place at the surface of grains and hence that detection could be done at not so high temperatures (400 ºC-500 ºC) [9].

SENSOR FABRICATION.

Pure titania and Nb-doped titania were prepared from alkoxides precursors via sol-gel route. The obtained materials were calcined at 600 ºC, 700 ºC, 800 ºC and 900 ºC. Materials calcined at 600 ºC and 700 ºC were chosen for sensors because their crystalline structure was mostly anatase.

The selected Nb-doped TiO_2 nanopawders were dispersed in glycerol and then a drop of the resulting paste was deposited manually over sensor electrodes. The as-deposited films were dried using a ramp of temperature with an increment of 20 ºC per minute to avoid cracks in the layer. Finally, the active layer was annealed for 2 hours.

Sensors were dried at 300 ºC and then ones were annealed at 600 ºC and others at 700 ºC. Drying and annealing processes were made in situ using the heater of the sensor. For the ramp of temperature, a ramp of voltage, proportional to heater resistance for each temperature, was applied to the heater employing a computer programmable power supply.

EXPERIMENT

To select the proper materials for sensors, XRD characterization of different calcined nanopowders was made using a Siemens D5000 X-Ray diffractometer.

For the characterization of the sensing properties, the sensor was connected into a test chamber (with a volume of 16 cm^3). In the first stage, pure nitrogen was input into the test chamber and the sensor base line was established. A constant flow of 200 ml/min was fixed to avoid interference of pressure in the measurements. Then a flow with nitrogen and oxygen was mixed with the pure nitrogen flux using mass-flow controllers. The accuracy of each mass-flow meter was +1 % of its full scale. Sensors were first tested at high concentrations of oxygen (10 %, 8 %, 6 %, 4 %, 2 %, 1 % and 1000 ppm), then they were tested at 1 ppm, 2 ppm, 5 ppm and 10 ppm of oxygen.

RESULTS

Based on XRD analysis (Fig. 1), it is possible to conclude that the maximum annealing temperature of doping material to ensure that a considerable quantity of material remains in anatase state is 700 ºC. Therefore, the maximum working temperature will be 600 ºC. In undoped material, the maximum annealing temperature to ensure that part of the material is in anatase phase is 600 ºC, and then in this case the maximum working temperature will be 500 ºC.

Dynamic response of doped material, calcined at 700 ºC, to high concentration (Fig. 2.) shows that behaviour of material to the presence of oxygen is typical, which in titania, a n-type material, is an increment of resistance of active layer proportional to the increment of oxygen levels.

Response of undoped material was not possible to appreciate with our measurement equipment because of the high resistivity of the active layer at

1000 ppm of oxygen. In both cases the working temperature was 500 ºC.

On the other hand, it was observed a clear response of the sensors to traces of oxygen (Fig. 3.), but in a not typical way. It seems that at this concentration of oxygen, the behaviour of the active material change from n-type to p-type. Working temperature of these measurements was also 500 ºC.

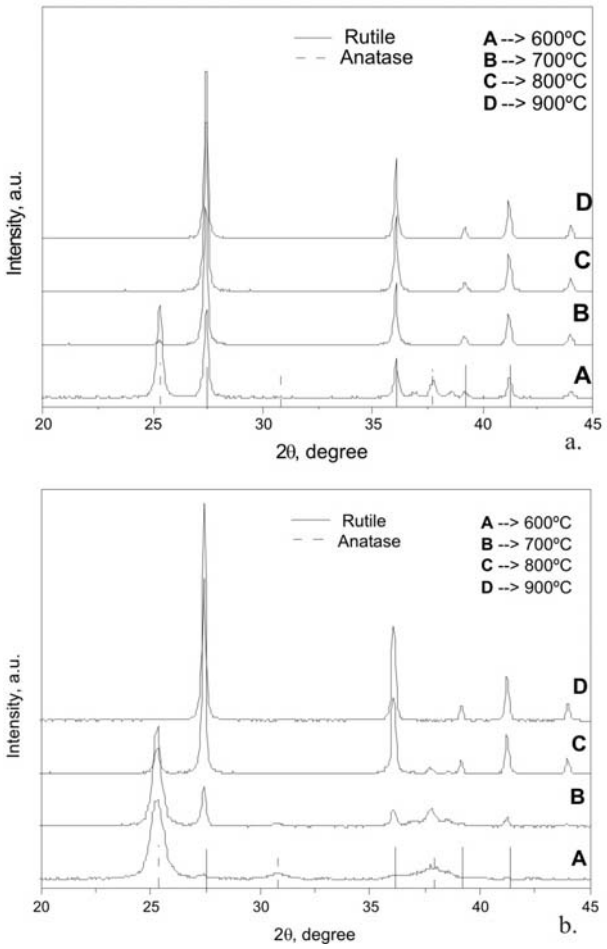

Fig. 1. XRD patterns of a. pure TiO_2 and b. TiO_2 doped with 3 at% of Nb.

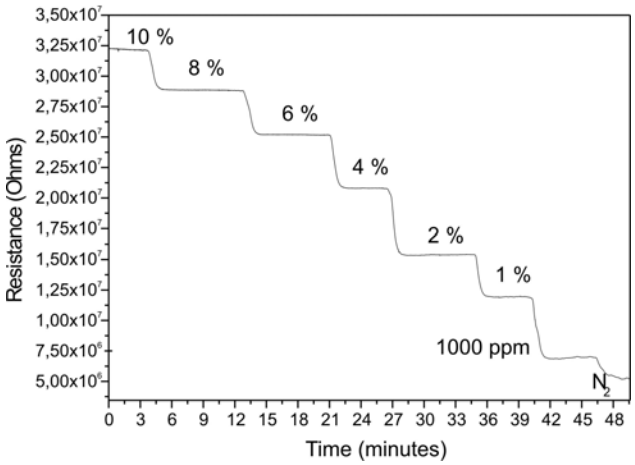

Fig. 2. Dynamic response of doped material cacined at 700ºC, to concentrations of O_2.

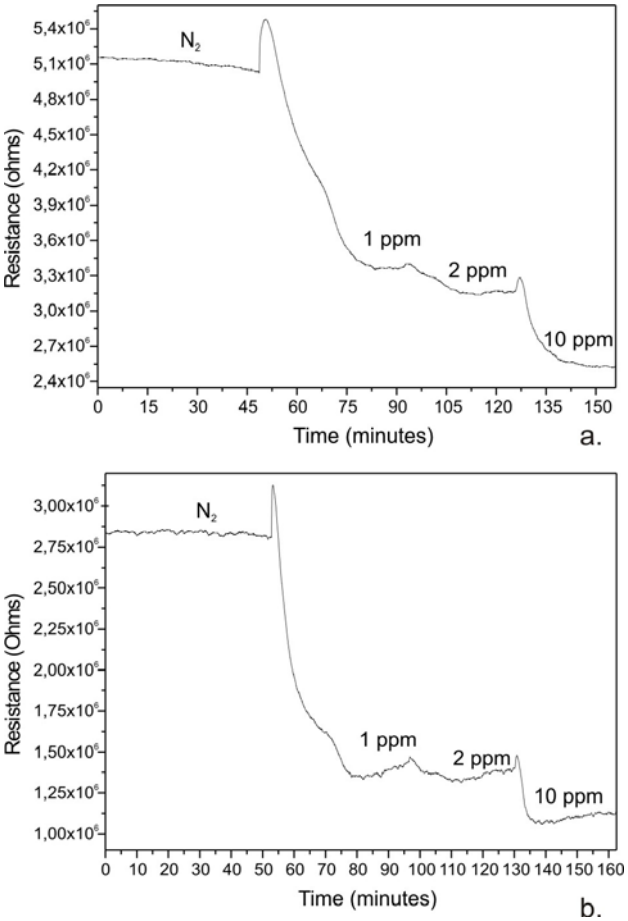

Fig. 3. Dynamic response of a. undoped material and b. doped material, cacined at 700 ºC, to traces of O_2.

REFERENCES

[1] http://www.aii1.com/applications.html

[2] R. K. Sharma, M.C. Bhatnagar; *Sensors and Actuators B* 56 (1999) pp 215-219.

[3] Y. Hu, O.K. Tan, J.S. Pan, H. Huang and W. Cao; *Sensors and Actuators B* (2004), in press.

[4] V. Guidi et al; *Sensors and Actuators B* 84 1 (2002) pp 72-77.

[5] R. K. Sharma, M. C. Bhatnagar and G. L. Sharma; *Sensors and Actuators B* 46 3 (1998) pp 194-201.

[6] U. Kiner, K.D. Schierbaum, W. Göpel; *Sensors and Actuators B* 1 (1990) pp 103-107.

[7] R. K. Sharma, M. C. Bhatnagar and G. L. Sharma; *Applied Surface Science* 92 (1996) pp 647-650.

[8] J. Arbiol, Doctoral thesis, Universitat de Barcelona, Departament d'Electrónica. 2001.

[9] Y. Xu, X. Zhou, O. T. Sorensen; *Sensors and Actuators* B 65 (2000) pp 2-4.

Characterization of the 1.54 μm emission from Er and Si clusters co-doped silicate

Y. Lebour[(a)], B. Garrido, P. Pellegrino, C. Garcia, J. A. Moreno and J. R. Morante
Dep. d'Electrònica, Universitat de Barcelona, Martí i Franquès 1, 08028 Barcelona, Spain.
[(a)]Telephone: ++34 934039176, Fax: ++34 934021148, and E-mail: lebour@el.ub.es.

Abstract

We present a characterization of the mechanism of energy transfer from Si nanoparticles (Si-nc) to Er^{3+} ions in different silicate glasses, namely soda-lime and aluminum silicates, and a comparison with silica. Modeling of the energy transfer between the absorbing Si particles and the nearby Er^{3+} ions was carried out in order to estimate the relevant physical parameters which describe the emission process.

1. Introduction

The emission around 1540 nm from Er^{3+} ions in a silica matrix drives great interest as it corresponds to the minimum attenuation in silica-based optical fibers. Thermally stable structures and besides a relatively long emission-lifetime (some ms) are the main reasons why silica wafers doped with Er and Si clusters have been shown as one of the promising approaches for the fabrication of waveguide optical amplifiers. Er emission at 1540 nm is largely enhanced via an excitation through the Si nanostructures. This feature led to the demonstration of optical gain in waveguide structures, where erbium-doped silicon-rich silicon oxide constitutes the active layer. Moreover, measurement of signal enhancement in channel wave-guides codoped with Si-nc and Er when pumping laterally has been reported by our group and co-workers [1].

In this work, we have explored the possibility to extend the mechanism of energy transfer from Si clusters to Er in different silicate glasses: soda-lime and aluminum silicates, and compared to silica. The interest in such composite glasses resides in their wide optical bandwidth at 1540 nm and large Er solubility.

2. Experiment

Ion implantation technique was used in order to introduce a uniform Si excess (5% or 15% atomic excess) inside the wafers. After a first step annealing, carried out in order to give, Er implantation was performed, several doses were chosen so that the resulting Er peak concentration could vary from $2x10^{19}$ up to $6x10^{20}$ cm^{-3}. Thermal treatment at low temperature has been performed to enhance the Er emission around 1540 nm. The luminescence characterization of these structures was carried out in a previous work [2].

The structural investigation on the codoped silicates by energy filtered electron microscopy has revealed that for high Si doses and the proper annealing conditions, the introduced Si excess precipitates in form of small Si grains, of few nanometers. This feature indeed is the ideal configuration to maximize the efficiency of the energy transfer mechanism. More details are given elsewhere [3].

Time-resolved PL characterization was carried out in order to explore the dynamic response of the system (Si-nc, Er). The measurements were performed by using Ar laser with excitation at 488 nm (resonant line with an absorption band of Er) or at 476 nm (out of resonance), in a large range of power. The laser beam was modulated by a rotating chopper with frequencies around 11 Hz. The 1540 nm Er emission was detected with a GaAs Hamamatsu photomultiplier and displayed on a two channel digitizing Tektronix oscilloscope. From these measurements, we extracted the integrated PL emission, and the rise and decay lifetimes by an exponential fit. Finally, we deduced the effective excitation cross-section of Er in these glasses.

3. Luminescence characterization

It is worth noticing that at 488 nm, Er^{3+} ions are pumped both directly and indirectly (via an energy transfer from Si clusters), whereas at 476 nm excitation (higher photon energy than the first one), its emission is only yield by indirect excitation. Figure 1 shows the variation of the Er signal versus the photon flux at these two wavelength, obtained from silica wafer codoped with 5% Si excess and an [Er]=$6x10^{20}$ cm^{-3}, the sample was annealed at 950 ^{o}C.

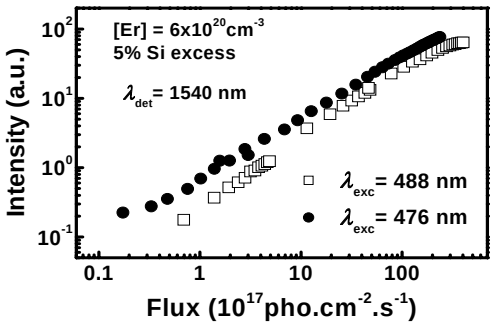

Fig. 1. PL intensity at 1.54 μm vs. the flux.

It is apparent that the (Si-nc, Er) system is more efficient when pumped out of resonant, it is to say that the direct-pumped Er emission is very weak due to its small absorption cross-section (about $4x10^{-21}$ cm^2), and is almost negligible here, as denoted also by the shape of the emission which is the same for the two kinds of excitation.

4. Modelization

Further study of the interaction between Er and Si particles was carried out by time-resolved PL characterization. We used a phenomenological model based on the Er energy level scheme, and given a rate equation describing the time evolution of the population N_{Er}^{*} of active Er^{3+} ions. This latter variable is increased by fast-transitions from upper levels of the Er^{3+} ion after they are indirectly-pumped from its fundamental level. It is proportional to the optically-active Er (with N_{Er} is the denoted total Er concentration), the effective excitation cross-section σ_{eff} and the pump flux ϕ. Then the rate equation governing the population of the first excited state of Er N_{Er}^{*} is

$$\frac{dN_{Er}^{*}}{dt} = \sigma_{eff}\phi\left(N_{Er} - N_{Er}^{*}\right) - \frac{N_{Er}^{*}}{\tau}. \qquad (1)$$

The last term in the right side of the equation represent the deexcitation processes with a lifetime τ including both radiatively, and thus the 1540 nm signal, and non-radiative, the well known concentration quenching effect involving closely situated Er^{3+} ions.

In this model: 1) we have neglected the 980 nm emission of Er, corresponding to transitions from the second excited state to the ground state, as we did not observed this signal in the whole range of power we used. 2) upconversion process, which is defined by energy transfer between two closely-situated excited Er ions, and Auger effect which is defined by energy transfer from excited Er^{3+} ion to an excited cluster, are neglected as these two processes are known to be more important at high pump photon flux. 3) this model can be applied regardless the host glass, the excitation wavelength (resonant or non-resonant), as far as the pump flux is not too high, i.e. second order phenomena, cited above, could be neglected. If this last condition is satisfied, the solution of the rate equation 1 is

$$N_{Er}^{*} = \frac{\sigma_{eff}\tau\phi}{\sigma_{eff}\tau\phi + 1} N_{Er}\left[1 - \exp^{-\left(\sigma_{eff}\phi + \frac{1}{\tau}\right)t}\right]. \qquad (2)$$

The exponential term of equation 2 provide a way to deduce the effective excitation cross-section by looking at the evolution of excitation (rise) time versus the flux. Indeed, the rise time of the Erbium excitation is given by

$$\frac{1}{\tau_{rise}} = \sigma_{eff}\phi + \frac{1}{\tau}. \qquad (3)$$

We note that the reciprocal of the rise time depend linearly on the photon flux ϕ. A plot of the inverse of the rise time should be a straight line, with σ_{eff} as its slope, and τ its intercept.

5. Time-resolved PL

A typical variation of the reciprocal rise time as a function of the photon flux is given in figure 2, which was obtained from a soda-lime sample co-implanted with 15 at.% Si excess and an Er concentration of $7x10^{19}$ cm^{-3}. We used a linear fitting procedure as given in eq. 3, and we estimated an effective cross-section about $1.27x10^{-17}$ cm^2 and an effective lifetime of about 5.92 ms. Moreover, for the whole studied samples we found that the effective excitation cross-section change byn a factor of 6 at most.

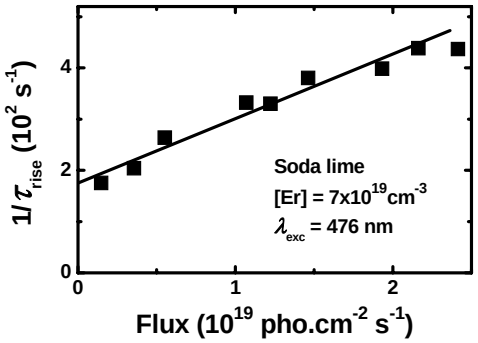

Fig. 2. Variation of the reciprocal of the rise time with the photon flux at 476 nm from soda-lime glass.

6. Conclusions

A modeling of the energy transfer in the (Si-nc, Er) system at low pump radiation was presented and provides useful parameters such as the PL effective excitation cross-section and lifetimes. We estimate lifetimes ranging from 2.5 to 12 ms (depending on the Er dose and Si excess) and an effective excitation cross-section about $1 x10^{-17}$ - $6 x10^{-17}$ cm^2. This is several orders of magnitude higher than the Er direct absorption cross-section (about 10^{-21} cm^2). This result provides an open route to improve even further the gain figures and waveguide characteristics of photonic devices based on the erbium/ nanosilicon system.

References

[1] N. Daldosso, D. Navarro-Urrios, M. Melchiorri, L. Pavesi, F. Gourbilleau, M. Carrada, R. Rizk, C. García, P. Pellegrino, B. Garrido, and L. Cognolato, Mat. Res. Soc. Symp. Proc. Vol. **832**, F11.3 (2005).

[2] P. Pellegrino, B. Garrido, Y. Lebour, J. A. Moreno, C. Garcia, J. R. Morante, P. Bettotti, L. Pavesi and M. Prassas, "Luminescent properties of Er and Si co-implanted silicates", Optical Materials **27**, 910 (2005).

[3] P. Pellegrino, B. Garrido, J. Arbiol, C. Garcia, Y. Lebour, and J.R. Morante, "Location of Er atoms with respect to Si nanoclusters in luminescent Er and Si co-implanted silicates", Mat. Res. Soc. Symp. Proc. Vol. **832**, F11.4 (2005).

Gas detection via advanced sensor matrices

P. Ivanov[1], F. Blanco[1], E. Llobet[1], X. Vilanova[1], I. Gracia[2], C. Cané[2], X. Correig[1]

[1] Dept. Electronic Engineering, University Rovira and Virgili, Tarragona, Spain.

[2] Dept. Microsystems and Silicon Technologies, National Center of Microelectronics, Barcelona, Spain.

1. Abstract

Among the many physical and chemical strategies used to make air pollution gas sensors for CO and NO_2 monitoring, those employing multi-sensor arrays offer excellent selectivity, long lifetimes, low drift and low costs of manufacture. Targeting the two gases CO and NO_2, new thick film sensor matrix was fabricated using the screen printing technology. With this purpose, undoped and noble metal-doped thick film SnO_2 sensing layers deposited by screen printing technique upon micro-machined Si substrate have been characterised.

2. Introduction

Greater part of the combustion processes result in the formation of nitric oxides, commonly considered inside the global label NO_x. Automobiles, industrial boilers, coal and natural gas power plants produce about 1:10 of NO_2 in the primary exhaust gases [1]. Nitrogen oxides and carbon monoxide have large importance on combustion control and consequences on health and environmental pollution. NO_2 and CO even at low concentration are highly toxic gases. Nitric oxides inhalation leads to pulmonary edema and death. Furthermore, NO_2 and CO catalyze the formation of toxic ozone in the troposphere, being one of the causes of the urban smog. These gases also participate in a chain reaction that destroys the protective stratospheric ozone layer, resulting in an increase of the ultraviolet radiation reaching the surface of the earth [2].

Metal oxide gas sensors are widely used devices for measuring gas emissions. However, the requirement of high working temperatures of such devices, has directed the development of gas sensors to the use of new silicon micromachined structures. In the present work, we study the sensing performances of 4 tin oxide sensors (pure and doped) integrated in a single sensor micro-hotplate matrix. The objective consists in obtaining a reliable and stable enough NO_2 gas sensor.

3. Fabrication of the sensor array

3.1 Micro-hotplate fabrication

The 4-element integrated micro-hotplates were fabricated on double-side polished p-type <1 0 0> Si substrates, 300 μm thick (4-40 Ω·cm). The structure of the device basically consists of the gas sensing layer, the electrodes, insulating layers and a polysilicon heater. The technological process needed to fabricate the sensors is described in [3]:

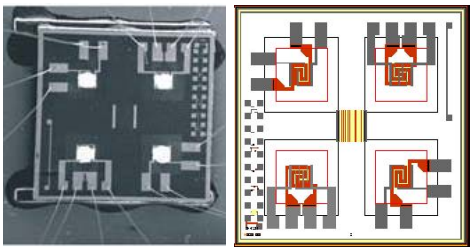

Fig. 1 Micrographs of tin oxide coated membranes (left). Electrode, heater and membrane configuration (right).

Each chip was mounted on a TO-8 package. Gold wires of 25 μm in diameter were used for standard ultrasonic wire bonding. Figure 1 shows micrographs of tin oxide coated membranes where the 4 membranes are clearly visible (left) and the electrodes, heater and membrane design (right).

3.2 Active film deposition

Based on previous experience, tin oxide was selected as active materials for sensing NO_2 and CO. The effects of including Pt, Pd and Au as metal catalysts were investigated. Using an adapted screen-printing technique, sensitive layers of pure and doped tin oxide were deposited [4]. The technological procedure reported here allows for depositing 4 different sensing layers before the membranes have been etched, which avoids damaging the membranes during film deposition and increases fabrication yield. The deposition method overcomes disadvantages such as low porosity and low surface area, generally associated to chemical vapour deposition or sputtering methods, and the fact that only the 4 membrane areas are heated keeps power consumption low (80 mW when working at 500°C).

4. Experimental

The fabricated devices were tested in the presence of three concentrations of NO_2 (1, 5 and 10ppm) and CO (1000, 2500, and 3500 ppm) at 3 different operating temperatures (250, 350 and 450ºC). Each measurement of a given species and concentration was replicated three times.

5. Results and discussion

5.1 Structural and compositional studies

The morphology and composition of the film was investigated by SEM. The thickness of the sensing layer was 5 μm and the particle size was around 40

nm. SEM analyses showed that the different doping did not affect the structure of the active layer. EDX analyses determined that the quantity of catalysts is in the range of 1-1,15wt%.

5.2 Gas sensitivity measurements

The fabricated devices have been tested in the presence of NO_2 and CO at 3 different temperatures (250, 350 and 450ºC) and for three concentrations using a continuous flow system.

Layer	T [ºC]	NO_2 (ppm)			CO (ppm)		
		1	5	10	1000	2500	3500
SnO_2	250	3.41	7.25	24.27	1.01	1.14	1.2
	450	1.42	1.93	2.91	1.12	1.25	1.31
SnO_2 +1%Au	250	**4.57**	**12.7**	**50.01**	1.35	2	2.2
	450	**2.71**	**5.23**	**10.36**	2.14	3.39	4.66
SnO_2 + 1%Pd	250	4.14	8.63	25.6	**1.52**	**2.25**	**2.48**
	450	1.37	3.49	5.96	**2.26**	**3.58**	**4.92**
SnO_2 +1%Pt	250	4.35	10.1	27.63	1.45	2.14	2.36
	450	1.49	3.8	6.2	2.07	3.28	4.52

Table 1 Sensor sensitivity to NO_2 and CO.

In order to obtain values >1, the sensor response was calculated as the ratio R_a/R_g (for CO) and R_g/R_a (for NO_2), where R_a is the resistance of the sensor in the presence of clean air and R_g is the sensor resistance in the presence of a diluted volatile.

The main objective of the gas sensitivity studies was to select the materials and catalysts to be used for detecting NO_2 and CO. Table 1 summarize the results of the gas sensitivity studies. The tested sensors showed good sensitivity to both of the target species, but at different temperatures. This behavior can be used to improve the selectivity of the sensors.

Among the different tin oxide sensors tested, the Au-doped SnO_2 sensors showed the highest response to NO_2. Their response was up to 2 times higher, than the response of un-doped SnO_2 sensors. Pd-doped tin oxide sensors showed best sensitivity to CO.

However, in the humidity tests the doping does not considerably affect the sensor performance.

5.3 Gas analysis using a 4-element integrated microarray

Qualitative and semi-quantitative analyses of the vapours were performed using principal component analysis (PCA) and a fuzzy ARTMAP neural network, respectively. These pattern recognition methods were implemented using standard functions from MATLAB.

For the analysis, the number of measurements was equal to 18, which corresponded to 2 gases (NO_2 and CO) measured at 3 different concentrations (i.e. 6 different combinations) and each combination was replicated 3 times.

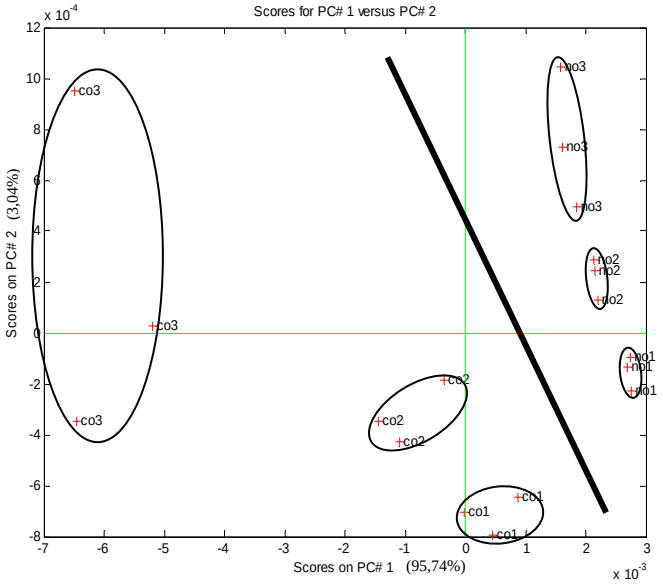

Fig.3 Results of a PCA performed on the responses of the 4-element integrated microarray.

Prior to perform a PCA, the data were mean-cantered. The PCA was performed using the responsesof the 4-element sensor microarray. For each measurement, the feature extracted from the response of each sensor within the microarray was the conductance change: $\Delta G = 1/R_g - 1/R_a$. The response features were gathered to form a response matrix, which had 4 columns (one column per sensor within the array) and 18 rows, which corresponded to the number of measurements in the dataset. Figure 3 shows the scores plot of the PCA. From the plot it could be observed that the responses to the two different types of gases could be easily separated (see the line on the plot). The first two principal components accounted for 98.78% of the variance in the data. Measurements belonging to the same vapour cluster together in the score plot.

6. Conclusions

From the results above, it can be seen clearly that the doping study allow us to select the optimal doped active layer for the desired application. By combining four sensors with different doping, together with the pattern recognition techniques, it is possible to discriminate between NO_2 and CO. These results verify the viability of the fabrication technique used in this study.

References

[1] C. Cooper, F. Alley, Air pollution Control, A Design Approach, Waveland Press, second ed., Illinois, 1994.

[2] N. Nevers, Air Pollution Control Engineering, McGraw-Hill, New York, 1995.

[3] M. C. Horrillo et al, Detection of low NO_2 concentrations with low power micromachined tin oxide gas sensors, *Sens. Actuat. B* 58 (1999) 325-329.

[4] E. Llobet et al, Screen-printed nanoparticle tin oxide films for high-yield sensor microsystems, *Sens. Actuat. B 96* (2003) 94-104.

MWNT and Hybrid MWNT/WO_3 Gas Sensors

E.H. Espinosa[1], R. Ionescu[1], C. Bittencourt[2], A. Felten[2], J. Calderer[3], X. Vilanova[1], J. Brezmes[1], X. Correig[1], J.J. Pireaux[2], E. Llobet[1]

[1]Departament d'Enginyeria Electrònica, Elèctrica i Automàtica, ETSE, Universitat Rovira i Virgili, Avda. Països Catalans, 26, 43007 Tarragona, Phone: 977 558764; Fax: 977 559605; e-mail: edwin.espinosa@urv.net
[2]LISE, Facultés Universitaires Notre Dame de la Paix, B-5000 Namur, Belgium
[3]Dept. Enginyeria Electrònica, Universitat Politècnica de Catalunya, Campus Nord, E-08034, Barcelona, Spain

Abstract

Multi-wall carbon nanotubes were functionalised under different conditions, with different chemical compounds (oxygen, ferrocene or acrylic acid). They were either drop-coated onto micro-hotplates or used to fabricate hybrid layers of functionalised MWNT and WO_3 combining drop-coating and r.f. sputtering methods onto alumina substrates. Scanning electron microscopy showed that a good coverage of the nanotubes by WO_3 could be reached. The responsiveness of our sensors operated at room temperature to air pollutants and toxic gases such as NO_2, NH_3 and CO was investigated.

1. Introduction

Carbon nanotubes (CNT) result advantageous for gas sensing because of their very large surface area and electronic properties [1, 2]. Another important property is that they are sensitive to gases at low temperatures (e.g. below 200ºC), and also at room temperature [3, 4], which reduces the power consumption of the device and enables the safe detection of flammable gases. However the presence of a thick graphite-like layer at the surface of the nanotubes, which contributes with sp^2 electronic states, can rule out the sensing potentiality of this material. Several methods, such as chemical, electrochemical and plasma treatment can be applied to modify the chemical composition of the nanotubes surface [5].

In this work we applied the drop coating method for depositing thick films of MWNT previously treated in different plasma (oxygen, acrylic acid or ferrocene) onto micro-hotplate substrates. Also we mixed MWNT with WO_3 to investigate the responsiveness of our active layers, operated at room temperature, to air pollutants and toxic gases such as NO_2, NH_3 and CO.

2. Materials

The CNT used were multi-wall carbon nanotubes produced by Nanocyl, purity higher than 95%. The as-provided CNTs were functionalised in a home-made chamber using inductive coupled plasma at the RF frequency of 13.56 MHz. The reactor consisted of a pyrex glass tube connected to a steel chamber. In order to perform a uniform functionalisation, the nanotubes were placed inside a glass vessel and a magnet, externally controlled from the plasma chamber, was used to stir the carbon nanotube powder during this treatment. The monomer (oxygen, acrylic acid or ferrocene) was then introduced in gas phase inside the plasma chamber via a needle valve. Table 1 summarises the parameters used.

Plasma	Power	Time	Name
Acrylic Acid	15W	15 min	5A
Ferrocene	15W	5 min	5B
Ferrocene	50W	5 min	5C
Acrylic Acid	50W	30 min	5D
Oxygen	30W	5 min	OxA
Oxygen	5W	5 min	OxB
Oxygen	5W	2 min	OxC
Oxygen	100W	5 min	OxD

Table 1. MWNT functionalisation

XPS and ToF-SIMS were used to monitor the change induced in the CNTs surface due to the plasma treatment. The type of functional groups was found to be related to the parameters used in the plasma functionalisation.

3. Experimental

We dispersed functionalised MWNT in glycerol employed as organic vehicle (in a ratio of 76 mg/l). The adequate homogenisation of the solution was reached by placing it in an ultrasonic bath at 75ºC for 2 hours. All materials were finally deposited by drop-coating onto micromachined substrates using a JBE1113 Dispenser (I&J FISNAR Inc., USA) and samples 5B, 5C, OxB and OxD were mixed with WO_3 by combining drop-coating and r.f. sputtering methods onto alumina substrates. For burning out the organic vehicle, a post-deposition process was necessary. For this, samples functionalised with oxygen were annealed in situ in air atmosphere at 400ºC for 2 hours by applying a constant voltage to their heating element. A 15 min. ramp was used to reach the annealing temperature. For other samples an important aspect had to be taken into account: the boiling point of ferrocene is 249ºC, and of acrylic acid was 141ºC. Thus we considered inappropriate to anneal these samples in order to avoid the burning of the chemical compounds

too. We opted instead for drying them at 110ºC for 24 to 48 hours in air.
The sensors were kept in a 5,3 l test chamber, where the contaminants (NO_2, CO and NH_3) were introduced by direct injection. The measurements were performed at ambient temperature.

4. Results

A SEM analysis of the resulting sensitive materials showed that well-adhered thick films of MWNTs were obtained (see Fig. 1up) and that in hybrid sensors, thin WO_3 layer covered the surface of carbon nanotubes (see Fig. 1down).

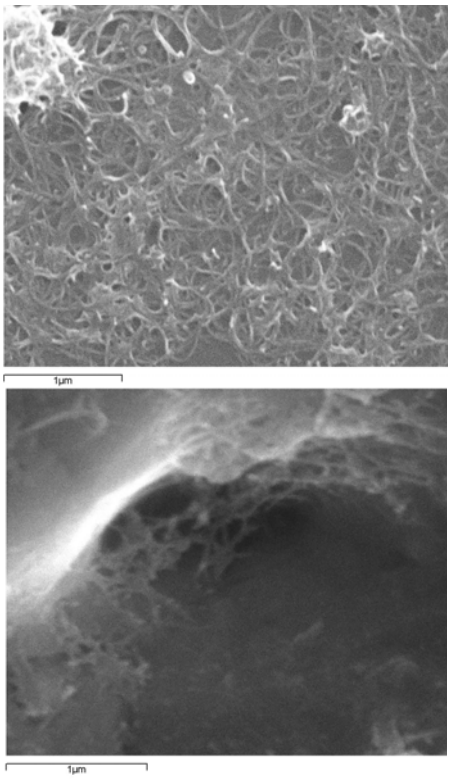

Fig.1. MWNT deposited over the sensor substrate. (up), MWNT covered by a 76 nm-thick layer of WO_3 (down).

NO_2 was the only gas to be detected by every active film studied. Sensors were able to detect NO_2 at the ppb level, (responded to a concentration of 100 ppb). The best response was obtained by the acrylic acid functionalised samples (Figure 2), while the responsiveness of the others active layers was lower and rather similar.

On the other hand, 10 ppm of CO could be detected only by samples functionalised with acrylic acid. Concentrations as high as 50 ppm of CO did not produce any response in the other active layers studied.

Hybrid samples 5B with 15 nm of sputtered WO_3 were the only sensors that could detect 10 ppm of NH_3 working at ambient temperature (Figure 3).

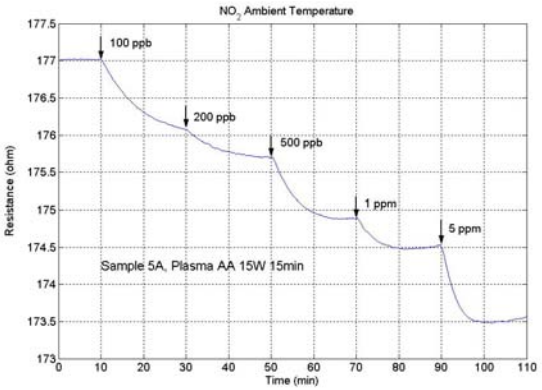

Fig.2. Responses at room temperature to increasing concentrations of NO_2 of sensor 5A.

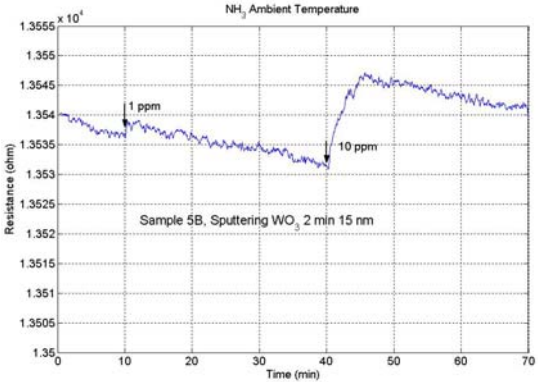

Fig.3. Hybrid sensor 5B with 15 nm of WO_3 response at room temperature 10 ppm of NH_3.

5. Conclusions

Different functionalisations (with oxygen, ferrocene or acrylic acid) of MWNT were tested for fabricating chemical gas sensors working at ambient temperature. The acrylic acid one was found to be the most suitable for NO_2 and CO, which detected 100 ppb of NO_2 and 10 ppm of CO. The combination of MWNTs and WO_3 thin films in hybrid sensors can improve the gas sensing properties of WO_3 based sensors operated at ambient temperature.

References

[1] M.S. Dresselhaus, et al., “Science of Fullerenes and Carbon Nanotubes”, Academic Press, San Diego, 1996.
[2] J. Che, et. al, “Studies of fullerenes and carbon nanotubes by an extended bond order potential”, Nanotechnology, 11 (2000), pp 65-69.
[3] R. Ionescu, et al., “Oxygen functionalisation of MWNT and their use as gas sensitive thick-film layers”, Sensors Actuators B, In press (2005), available online.
[4] S. Chopra et al., “Selective gas detection using a carbon nanotube sensor”, App. Ph. Lett., 83 (2003), no. 11, pp 2280-2282.
[5] A. Felten et al, “Oxygen functionalized MWNT as active layer for gas sensing: Detection of NO2 and NH3”, AVS 51st Internat. Symposium & Exhib., Anaheim (USA), Book of Abstracts, pp. 109, 2005.

One-dimensional porous silicon photonic crystals for 1.55 μm applications

E. Xifré Pérez, J. Ferré Borrull, L.F. Marsal and J. Pallarès

Departament d'Enginyeria Electrònica, Elèctrica i Automàtica, ETSE, Universitat Rovira i Virgili. Avda. dels Paisos Catalans, 26, 43007 Tarragona, Spain. E-mail: exifre@urv.net

Abstract

In this article, we will theoretically demonstrate that porous silicon is a suitable material for the formation of one-dimensional photonic crystals. Porous silicon distributed Bragg reflectors (DBR) with a band-gap centered at 1.55 μm will be designed. Besides, we will mathematically demonstrate that porous silicon is a suitable material for the design of microcavities with a transmission peak centered at 1.55 μm.

1. Introduction

A great deal of interest has been generated in photonic crystals because of their peculiar properties [1]. Photonic crystals are structures made of periodic dielectric media that posses photonic band gaps, that is, ranges of frequency in which light can not propagate through the structure. The existence of the spectral gap in photonic crystals opens up a variety of possible potential applications such as thresholdless semiconductor lasers, efficient optical filters, omnidirectional mirrors [2,3], etc.

Alternating layers of dielectric material with different refractive indices are the simplest possible photonic crystals known so far [4]. These one-dimensional photonic crystals are known as multilayers. A very interesting material for the fabrication of multilayers is porous silicon. Porous silicon can be obtained by HF electrochemical etching of silicon, which generates a range of refractive indices by changing the value of the current density during the anodization process. The thickness is determined by the time during which the current is applied [5]. It has excellent mechanical and thermal properties and is obviously compatible with silicon-based microelectronics.

The range of refractive indices obtainable with the formation technique of porous silicon depends on different fabrication parameters, especially on the electrolyte composition (HF concentration) and the resistivity of the wafers. The refractive index of porous silicon may range from 1.2 [6] to 2.7 [7], approximately. The thickness of porous silicon layers may range from tens of nanometers to micrometers [6].

In this paper, we theoretically study the suitability of porous silicon for the design of multilayers for 1.55 μm applications. We will present the simulation results of distributed Bragg reflectors and microcavities, using the range of refractive indices obtainable with the formation technique of porous silicon.

2. Multilayer structures

One-dimensional photonic crystals are made of the periodic repetition of different refractive index layers. Each period consists of two layers with refractive indices n_1 and n_2, and thickness h_1 and h_2, respectively.

The propagation of electromagnetic radiation in this layered medium can be solved by the transfer matrix method [8]. All the results obtained in the next section have been calculated using this extended method.

3. Applications

Although one-dimensional photonic crystals are very simple structures, they have many applications. We present the design and the simulation results of two possible applications based on porous silicon: distributed Bragg reflectors and microcavities, both for 1.55 μm applications.

3.a. Distributed Bragg Reflectors.

Distributed Bragg Reflectors (DBR) are multilayers where the optical thickness of the two periodic layers is given by $n_1h_1 = n_2h_2 = \lambda/4$. This structure presents a high reflectance band (band-gap) centered at approximately l. The thickness of the layers can be calculated as $h=\lambda/(4*n)$. For λ=1.55 μm applications, the calculated thickness for any refractive index obtainable with porous silicon is of hundreds of nanometers. Therefore, it is possible to deduce that porous silicon is a suitable material for the formation of DBR for 1.55 μm applications. Figure 2 shows the reflectivity spectra of a few DBR whose band-gap is centered at 1.55 μm.

It can be observed that the width and the sharpness of the band-gap depend on two parameters: the n_1/n_2 ratio (Figure 1a) and the number of periods N of the multilayer (Figure 1b) when the other parameters

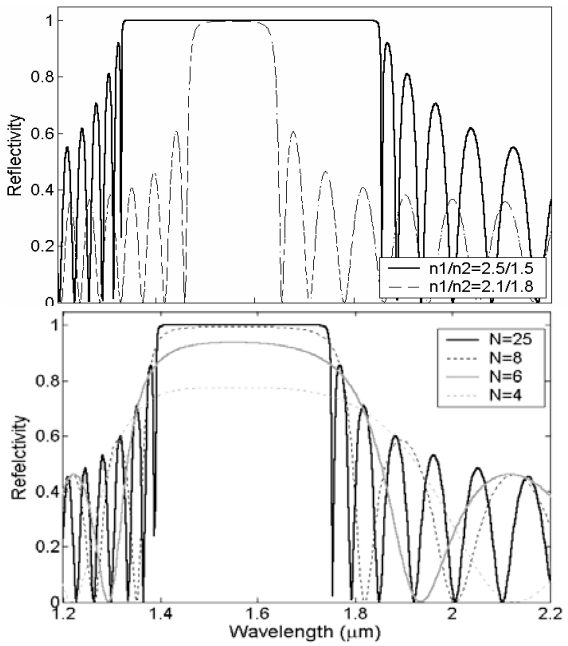

Fig.1. Reflectivity spectra of multilayers used as a DBR for λ=1.55 μm (a) with different n_1/n_2 ratio and N=25 periods; (b) with n_1=2.4, n_2=1.7, h_1=161.6 nm and h_2=228 nm, with different number of periods N.

remain constant. It can be observed that, the higher the ratio n_1/n_2 the widest the band-gap and that when the number of periods N increases, the filter is more abrupt and the reflectivity inside the band-gap tends to unity exponentially with N.

3.b.- Microcavities.

Microcavities are generally obtained by inserting a defect layer in between two symmetric $\lambda/4$ Bragg reflectors. The optical thickness of the defect is usually $\lambda/2$ or λ.

The reflectivity spectrum of a microcavity centered at 1.55 μm can be observed in Fig. 2. The inset in this figure shows the schematic structure of a microcavity. The refractive index of the defect layer may be lower than the refractive indices used for the DBR or equal to the lowest refractive index of the DBR. For this example, a lower refractive index for the defect layer has been chosen, n_d=1.35, being n_1=2.4 and n_2=1.7. The thickness of the layers have been calculated using the expressions $n_1h_1=n_2h_2=\lambda/4$ and $n_dh_d=\lambda$.

The width of the transmission peak at λ depends on the number of periods N of the Bragg reflectors of the microcavity. This influence can be observed at the reflectivity spectra of the multilayers in Fig. 2. The peak centered at λ=1.55 μm is narrower when the number of periods N increases. However, the number of periods N is limited because the increase of N results in a narrower peak up to a certain N, from what the transmission of the peak begins to reduce, until it disappears.

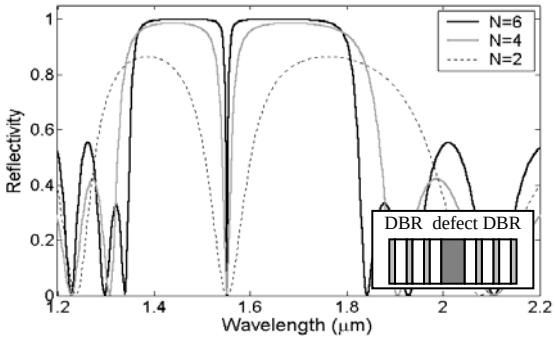

Fig.2. Reflectivity spectra of a microcavity consisting of two symmetric DBR with n_1=2.4, n_2=1.7, h_1=161.6 nm and h_2=228 nm, and with a defect layer n_d=1.35 and h_d=575 nm. The transmission peak is centered at 1.55 μm.

4. Conclusions

The optical response of multilayer structures is determined by the refractive index, the thickness of the layers and the number of periods of the structure. In this work, two porous silicon multilayer structures have been presented: distributed Bragg reflectors (DBR) and microcavities. We have shown that porous silicon is a suitable material for the formation of these structures for 1.55 μm applications. For the DBR, it has been demonstrated that the higher the ratio between the two refractive indices used for the multilayer, the wider the band-gap. It has been also shown that the higher the number of periods N of the DBR, the sharper the edges of the band-gap.

A microcavity with a transmission peak centered at 1.55 μm has also been designed. The influence of the number of periods of its symmetric DBRs on the width of the transmission peak has been discussed. The increase of the number of periods N leads to a narrower transmission peak, although this number N is limited in order not to make the peak disappear.

References

[1] S.K. Srivastava, S.P. Ojha, "Operating characteristics of an optical filter in metallic photonic bandgap materials", Microwave and Optical Tech. Lett., 35, 68-71 (2002).

[2] E. Xifré Pérez, J. Pallarès, L.F. Marsal, J. Ferré Borrull, "Porous silicon mirrors with enlarged omnidirectional band-gap", J. Appl. Phys., 97, 064503 (2005).

[3] E. Xifré Pérez, T. Trifonov, J. Pallarès, L.F. Marsal, "One-dimensional porous silicon photonic crystals for visible and NIR applications", Phys. Stat. Sol., 2, 3466-3470 (2005).

[4] V. Agarwal, J.A. del Rio, "Tailoring the photonic band gap of a porous silicon dielectric mirror", Appl. Phys. Lett., 82, 1512-1514 (2003).

[5] A. Bruyant, G. Lérondel, P. J. Reece, and M. Gal, "All-silicon omnidirectional mirrors based on one-dimensional photonic crystals", Appl. Phys. Lett., 82, 3227-3229 (2003).

[6] L. Pavesi, C. Mazzoleni, "Controlled photon emission in porous silicon microcavities", Appl. Phys. Lett., 67, 3280-3282 (1999).

[7] S. Chan, P.M. Fauchet, "Tunable, narrow, and directional luminescence from porous silicon light emitting devices", Appl. Phys. Lett., 75, 274-276 (1999).

[8] P. Yeh, Optical Waves in Layered Media, Wiley, New York (1988).

Enhancing sensor selectivity through flow modulation

C.Durán[1,2], J. Segarra[1], J.Brezmes[1], E.Llobet[1], X.Vilanova[1] and X.Correig[1]

[1]Dept. de Enginyeria Electrònica. Universitat Rovira I Virgili. Av. Països Catalans, 26. 43007 Tarragona (Spain).
[2]Departament of Electronic Engineering, University of Pamplona, Pamplona, Colombia
Tel: +34977 559619 Fax: +34977559605 e-mail: cristhian.duran@urv.net

Abstract

In this paper, a new method to enhance sensor selectivity is described. A flow modulation system, driven by a PC-controlled peristaltic pump, has been designed to feed a sensor chamber with different vapors. 45 measurements where performed comprising five different species (benzene, toluene, o-xylene, methanol and para-xylene) in three different concentrations (20, 200, 2000 ppm). Using frequency domain techniques and neural networks, the system was able to reach a 92% classification success rate when identifying all five vapors despite concentration was not constant and a single sensor was used.

1. Introduction

In the last ten years, considerable efforts have been made to use sensor dynamics as a source of multivariate information leading to an enhancement in the discriminating ability of poorly-selective metal oxide gas sensor arrays. Many authors have reported on strategies based on modulating either the sensor operating temperature [1] or the analyte concentration [2,3]. Here we introduce and demonstrate, for the first time, a simple method that, combining simultaneously both effects, has the potential of increasing the resolving power of metal oxide sensors. Furthermore, its simplicity makes it especially suited for low-cost applications.

The approach involves a flow modulation of contaminated air through the sensor chamber. In this manner temperature and concentration modulations are achieved indirectly. By changing flow rate periodically, local differences in the concentration of the species being measured are generated. Moreover, surface temperature changes as the refrigeration effect of air flow is proportional to the flow rate applied.
Section 2 describes the experimental set-up, while section 3 describes the measurements performed and discusses the results obtained. Finally, section 4 outlines the conclusions and describes future work in this direction.

2. Experimental set-up

To achieve a flow-modulation capable electronic nose, we designed a closed loop system, based on a PC controlled peristaltic pump. Figure 1 shows the configuration devised.

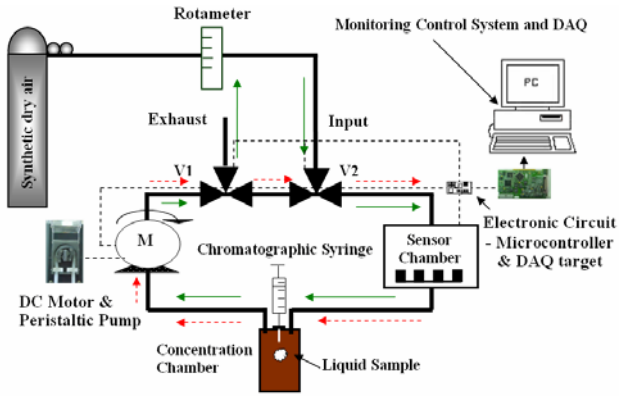

Figure.1. Schematic diagram of the flow modulation system.

The system has two operating modes. In the cleaning configuration, synthetic dry air enters the system through the first electro-valve and cleans the peristaltic pump, the sensor chamber and the evaporation chamber. Solid arrows mark the flow of clean air in this mode.
In measuring mode, air re-circulates around a closed circuit. Once the modulation is initiated, a chromatographic syringe sprays a calculated quantity of liquid contaminants into the evaporation chamber. Clean air inside the circuit becomes contaminated when forced to re-circulate around the evaporation chamber thanks to the peristaltic pump. Dashed arrows show this circuit.
A microcontroller commands the speed of the peristaltic pump which directly translates into different flow rates. A PC programmed with a written-in-house user friendly program communicates with the microcontroller so that the user can select the frequency and flow rate waveform that has to be

applied. Moreover, through this program, the PC commands the microcontroller to open or close the electro-valves to change the configuration of the system depending upon the operating mode desired.
Moreover, the PC records the sensor response (in terms of conductivity) and applies signal pre- and post-processing algorithms to identify the vapor sample measured.
Liquid quantities of the contaminants measured were calculated and sprayed into the contaminants chamber using a chromatographic syringe. A total of 45 measurements were performed. The measurements comprised five different vapors (benzene, toluene, methanol, *o*-xylene and para-xylene) at three different concentrations (20,200,2000 ppm) with three replicates for each type of measurement.

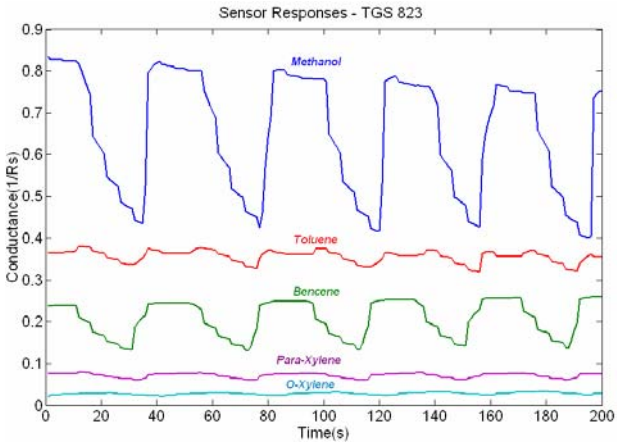

Figure.2. Typical responses with 5 contaminants.

Then, a periodic pulse modulation with a frequency of 10 mHz and an amplitude of 250 sscms was applied. Figure 2 shows a typical response from a sensor to five different contaminants when flow is pulsed as described above.

Sensor	Main application
TGS 800	Air Quality control
TGS 822	Alcohol detection
TGS 823	Organic Dissolvent

Table1. Sensors used and their main applications

Three different sensors were used for the measurements. Table 1 lists their designation and main applications. Their information was never combined to obtain better results, since the main goal of the experiment was to determine how selective each single sensor could get by itself using the flow modulation approach.
An FFT was applied to the periodic response and its amplitude value was considered. Values for the fundamental and harmonic frequencies were used as output data from the sensors and fed a Fuzzy Artmap pattern recognition algorithm.

3. Results and discussion

All results obtained and listed in Table 2 were performed using a cross-validation of order 1 (the so-called leave-one-out approach). The goal was to classify measurements in five different categories, one for each contaminant , with the added difficulty of variable concentration (20, 200 and 2000 ppm).

Pre-processing	TGS 800	TGS 822	TGS 823
None	84.44%	93.33%	91.11%
Mean centring	82.22%	82.22%	80.00%
Auto-scaling	53.33%	62.22%	55.55%

Table2. Classification rate for normalization strategy

Different preprocessing strategies were used to determine how much the mean amplitude, variance and waveform from each sensor response contributed to the classification of the 45 measurements.
From the results exposed in table 2 it is clear that best results are obtained when the evolution of sensor conductance through time is not preprocessed.
Anyhow, considering that classifying samples into 5 categories at random would yield a 20% success rate, it is clear that sensor response without mean value or even unbiased and scaled by its variance still retain useful information since classification rates never fail below a 53%.

4. Conclusions

A new modulation method has been tested to increase sensor selectivity. A wide range of concentrations and contaminants have been tested confirming that flow modulation allows for a reliable identification of different vapor species.
Additional work has to be done to optimize the system and test the approach under tougher conditions like binary or tertiary vapor mixtures.

References

[1] Llobet, E.; Brezmes, J.; Ionescu, R.; Vilanova, X.; Al-Khalifa, S.; Gardner, J.W.; Bârsan, N.; Correig, X. "Wavelet Transform and Fuzzy ARTMAP Based Pattern Recognition for Fast Gas Identification Using a Micro-Hotplate Gas Sensor", Vol: 83, pp. 238-244, 2002.
[2] E. Llobet, X. Vilanova, J. Brezmes, J.E. Sueiras and X. Correig, "Transient response of thick-film tin oxide gas sensors to multicomponent gas mixtures" Sensors and Actuators B, Vol: 47, pp. 104-112, 1998.
[3] E.Llobet, X.Vilanova, J.Brezmes, R. Alcubilla, J. Calderer, J. Suerias and X. Correig, "Conductance-transient analysis of thick-film tin oxide gas sensors under successive gas-injection steps", Meas. Science and Technology, Vol: 8, pp. 1133-1138, 1997.

Development of miniaturized benzene preconcentrator

F.Blanco, P.Ivanov, M.Vinaixa, X. Vilanova, X.Correig
Departament d'Enginyeria Electrònica, Elèctrica i Automàtica, Universitat Rovira i Virgili
Tarragona, Spain

Abstract

In this paper, we showed the investigation performed with a miniaturized benzene preconcentrator. It was based on adsorbent layer of Carbopack X (25 μg) developed on an alumina substrate, with which high concentration factor was obtained.

1. Introduction

Nowadays, the monitoring of volatile organic compounds (VOCs), that can cause a range of adverse health effects has received a great deal of attention. Benzene, in particular, has been shown to be an important carcinogen in studies of human health. It is present in outdoor and indoor environments. As part of the Air Quality Framework Directive of the European Union (Directive 96/62/EC), the "Daughter" Directive (Directive 2000/69/EC) for benzene sets the annual mean limit value at 5 μg m^{-3}, standardised to 293 K and 101.3 kPa [1]. The benzene is included in the known chemical group of aromatic compounds. For the detection of this type of gases, different techniques has been developed, mainly based in gas chromatography, combined with preconcentrator systems to be able to detect low concentrations.

Recent studies have showed that adsorption of benzene can be significantly improved by using graphitized carbon blacks such as Carbograph 5, Carbopack B or Carbopack X [2].

2. Process of fabrication

2.1 Selecting the adsorbent

There are varieties of adsorbents used in the field of thermal desorption. Often, choosing the right adsorbent can be difficult.

The relative difference between the adsorbents is based on their capability to efficiently retain and release an analyte. Normally, adsorbents qualified as “too strongly adsorbed” means that adsorbent retains the analytes to the point that they are not efficiently released from the adsorbent during desorption and a portion of it can be observed if subsequent desorption is practiced. Where as, “irreversible adsorption” indicates the analyte can not be released from the adsorbent, and is not observed in the second desorption.

Recoveries of 80% or greater are typically considered acceptable in most thermal desorption methods. Recoveries between 21 and 79 % indicate a significant amount of the analyte was recovered from the adsorbent, but warns the user that break through occurred or that the analyte is too strongly retained. A recovery of less then 20 % is simply not suitable for any sampling application [3].

For our application, the adsorbent selected is Carbopack X. It has a surface area 240 m^2/gr, desorption temperature reaching 330ºC and excellent affinity to benzene.

2.2 Substrate fabrication

Preconcentrator substrates were fabricated by thick-film technology on an alumina substrate. In the first stage, we deposited heater and the temperature sensor using a commercial platinum paste (Heraeus C3657) and, after drying, we deposited the gold pads. Then they were all fired at 875 ºC. The typical value of the temperature-measuring resistor was 15 Ω ± 5% and the value of the heating resistor was 10 Ω ± 3% with a low temperature coefficient of approximately $3.45.10^{-3}ºC^{-1}$ for temperatures between 25 ºC and 350 ºC.

2.3 Fabrication of the preconcentrator

Using screen-printing technique, layers of TEMPFLEX 5145 (Loctite, is a non-corrosive adhesive, the single part paste offers excellent adhesion to ceramics, which retains its characteristics over a wide temperature range resisting long term exposure at 250°C), were deposited on alumina substrates. After this, 25 μg de Carbopack X is added in order to create the absorbent layer with area of 16 mm^2. The structure of the fabricated concentrator is shown on Fig 1.

The procedure of carbon activation consisted in annealing them in nitrogen atmosphere at 250 ºC for 2 hours.

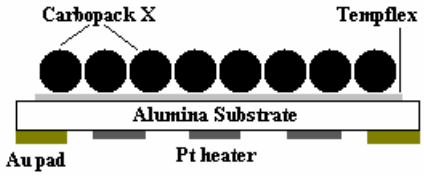

Fig. 1 Schematic diagram of the integrated concentrator

3. Results and discussion

3.1 Structural studies

The morphology and composition of the screen-printed sensing layers was investigated by scanning electron microscopy (SEM) and energy-dispersive X-ray spectroscopy (EDX). The specimens were coated

previously with a thin (around 20 nm) gold layer, which was sputtered on top of the samples to avoid charging effects. Specimens were observed at accelerating voltages 20 kV using a JSM 6400 field emission scanning electron microscope.

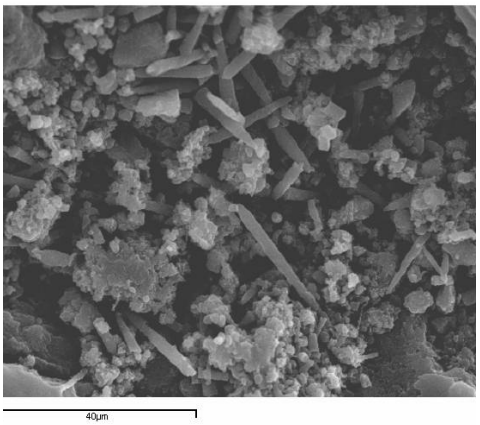

Fig. 2 SEM micrograph of the carbon structure.

The thickness absorbent layer was approximately 400 µm and the particle size was around 320 µm. The SEM analysis showed that absorbent layer is highly porous (Fig. 2).

3.2 Measurement system

For the characterization of the concentration factor of the fabricated preconcentrators GC/MS Shimadzu QP-5000 equipment has been used. In order to able to make the experiments, in it entrance a valve of 6 ways has been incorporated. A schematic view of the measurement system could be observed on Fig. 3.

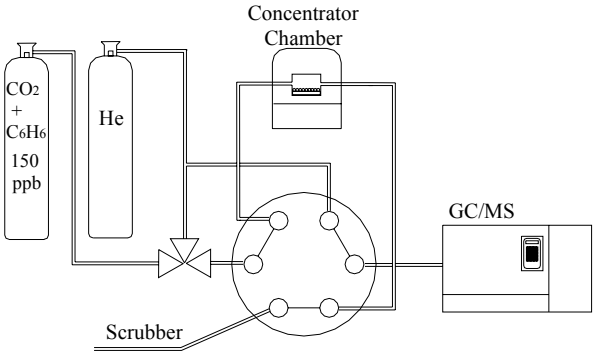

Fig. 3 Measurement system

3.3 Adsorption measurements

The measurement process was compound by the following two parts. At the beginning, a monitoring of the bottle concentration was performed. It consisted in five consecutive measurements called blanks. The values obtained permit us define the average benzene concentration in the calibrated bottle. In the next step, a series of tree adsorption/desorption processes, using the miniaturized preconcentrator, was made. On Fig. 4 a typical chromatogram of desorption could be observed. The small peak corresponds to the blank of the bottle.

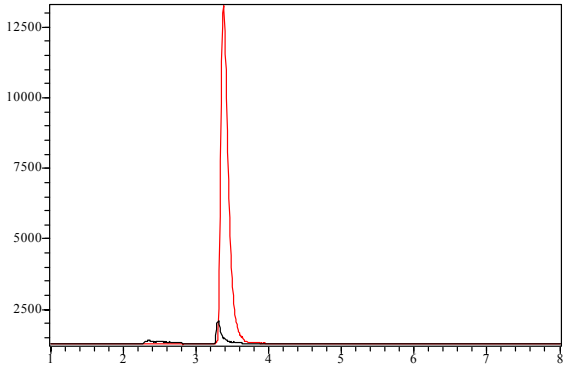

Fig. 4 Typical chromatogram of blank/desorption.

Comparing the average peak values obtained from the blank and desorption, the concentration factor could be calculated. In our case, the average concentration factor (based on 5 preconcentrators) reached 35 times. A sample results from the measurements of the blanks and preconcentratos is presented in Table 1.

Table 1Measurement results.

	Quantifying masses m/z	Peak integrated area
Blank 1	**78**	**3551**
Blank 2	**78**	**2050**
Blank 3	**78**	**2101**
Blank 4	**78**	**2099**
Blank 5	**78**	**2239**
Desorption 1	**78**	**82184**
Desorption 2	**78**	**86534**
Desorption 3	**78**	**69284**

4. Conclusions

The results obtained with the fabricated miniaturized preconcentrators showed high repeatability. The small size of the manufactured devices enables their incorporation in an integrated GC/MS-Gas sensors system.

References

[1] N. Martin et al, Studies using the sorbent Carbopack X for measuring environmental benzene with Perkin–Elmer-type pumped and diffusive samplers, *Atmospheric Environment* 37 (2003) pp. 871-879

[2] B. Strandberga et al, Evaluation of two types of diffusive samplers and adsorbents for measuring 1,3-butadiene and benzene in air, *Atmospheric Environment,* (2005)Article in Press

[3] J. Brown, A tool for selecting an adsorbent for thermal desorption application, SUPELCO Technical report (2001)

Contribution to the selection of Temperature Modulation Frequencies for Metal Oxide μ-Hotplate Gas Sensors using Multi-Level PRS

A.Vergara*, E. Llobet

Dept. Electronic Engineering, Universitat Rovira i Virgili
Av. Països Catalans, 26, 43007 Tarragona, Spain.
*alexander.vergara@urv.net

Abstract

A great deal of work has been done in the last decade towards mimicking the olfactory system of mammals with artificial systems: the so-called electronic noses. Even though gas sensors used in electronic noses give good results for gas detection, they still suffer some shortcomings as lack of selectivity or response drift. There are several techniques as thermal modulation to tackle these troubles.

In this paper a method based on multi-level pseudo-random sequences (ML-PRS) for modulating the working temperature of metal oxide micro-hotplate gas sensors in a wide frequency range is defined. This method helps in identifying each gas-sensor/system and in finding those modulation frequencies important for discriminating and quantifying different pollutant gases.

1. Introduction

The use of metal oxide based semiconductor gas sensor arrays on electronic noses is a well-established methodology. However, even though microhotplate gas sensors are inexpensive and very sensitive to different toxic species, they still suffer serious shortcomings such as poor selectivity and response drift.

Among the different strategies used to overcome these problems, thermal modulation of gas sensors has been a remarkably successful technique in many applications. Although the results reached were very promising, the selection of the modulation frequencies used until now, were not performed in a systematic way. Because of this, in a previous work [1], a systematic method to choose the modulation frequencies of micro-hotplate gas-sensors based on MLS pseudo-random binary sequences was presented.

In this paper, a method based on the temperature modulation in a wide frequency range of WO_3 microhotplate gas sensors is presented. This method is based on maximum length multi-level PRS instead of binary signals. This method helps to identify each gas-sensor system and to find, in a systematic way, the modulation frequencies important to discriminate between different gases and to estimate gas concentration.

2. Multi-level PRS and thermal modulation

The theory behind the generation of ML-PRS inputs for system identification is well developed. As in binary PRS, ML-PRS signals are periodic, deterministic signals, and have an autocorrelation function similar to white noise. ML-PRS exist for the number of levels, q, equal to a prime or a power of a prime $p(>1)$, i.e. for q = 2, 3, 4, 5, 7, 8, 9, 11, 13, ... (Zierler, 1959), [2]. The length of such a sequence $\{x_r\}$ is q^n - 1, where n is an integer. ML-PRS signals are generated in a similar manner that the PRBS using a shift register and modulo addition. Figure 1 shows the shift register configuration for ML-PRS generation, where we can see that $\{x_r\}$ are integers 0, 1, ..., (q - 1).

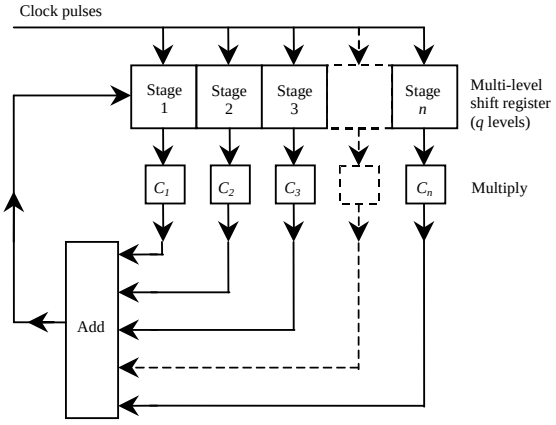

Fig.1. Multi-level PRS generation algorithm

The sequence can be thought of as being generated by a q-level shift register with feedback to the first stage consisting of the modulo q sum of the outputs of the other stages multiplied by coefficients c_1, ..., c_n which are the integers 0, 1, ..., (q - 1).

An estimate of the impulse response, h(t), of each sensor in the presence of pollutant gases was computed through the circular cross-correlation of one period (L = 624 samples) of the m-level PRS signal, x(t), and one period of the sensor response (i.e. resistance transient), y(t). The clock frequency of the m-level PRS was set to fc = 2 Hz and the sampling rate of the acquisition system was set to 10 Hz.

3. Experimental set-up

Vapours of 3 different concentration of NO_2 (0.5, 1, 2 ppm) and NH_3 (100, 500, 1000 ppm) and theirs binary mixtures diluted in synthetic air were measured while the working temperature of the micro-hotplates was modulated. Each measurement was replicated 5 times. These replicates (i.e. gas and concentration 30 measurements) were employed to find and select the modulation frequencies for gas identification and quantification (selection set). Figure 2 shows the typical ML-PRS signals used to modulate the sensor temperature and a typical response of micro-hotplate gas sensor (top to bottom).

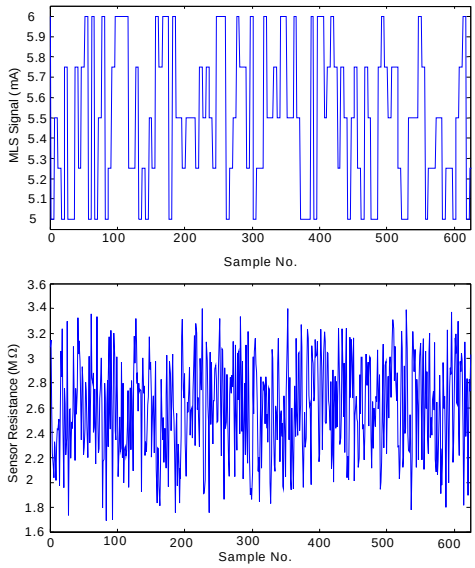

Fig. 2. ML-PRS applied to the heater element (top) and resulting resistance of a WO_3 micro-hotplate sensor in the presence of 2 ppm of NO_2 (bottom).

The sequences were decimated by 5 before the impulse response estimate was computed. The absolute value of the fast Fourier (FFT) of the impulse response estimate was calculated and stored for frequency selection by a variable selection process. Those frequencies selected correspond to those frequencies important for identifying and quantifying the gases.

Once the best modulating frequencies have been selected (using the ML-PRS), a multi-sinusoidal modulating signal is synthesized, applied to the sensors and the measurements are repeated.

4. Results and discussions.

A typical multi sinusoidal signal applied to the heater of the gas sensors is shown in figure 3 (top) and the absolute value of the FFT with values of the d.c. component and the 5 harmonics corresponding to the modulating frequencies at 2 ppm of NO_2 is showed on the bottom part of the same figure 3.

For both cases, one matrix per sensor was formed with the spectral components selected. These matrices were then used to build and cross validate by a LOO method a fuzzy ARTMAP NN classifiers in order to see whether it was possible to correctly identify and quantify the gases. The success rates for gas identification, varied between 78 to 98 % using a single sensor. On the other hand the success rate was from 87 % and up to 93 % when quantifying using only one sensor, and up to 100 % combining sensors.

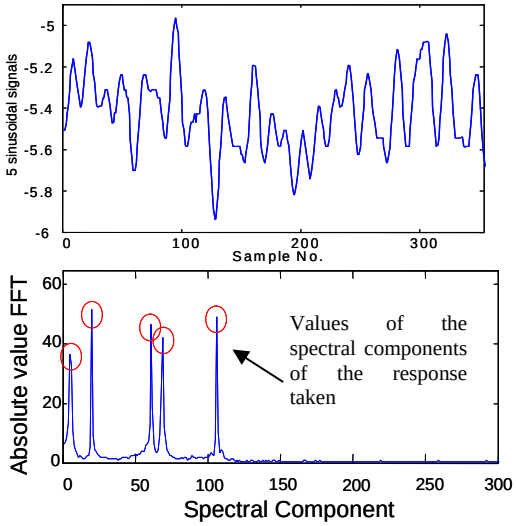

Fig. 3. 5-sinusoidal signal applied to the heater element (top) and resulting absolute value of the FFT in presence of 2 ppm of NO_2 (bottom).

A different way to optimize the gas sensor response can be obtained by a different method that consist in applying the phase space to a segment of the gas sensor response, while the working temperature is modulated [3]. Figure 4 shows the trajectories plotted in the phase space, when the method is applied to a segment of the gas sensor response at 3 different pollutant gases. Actually, on these trajectories, differences between responses can be observed.

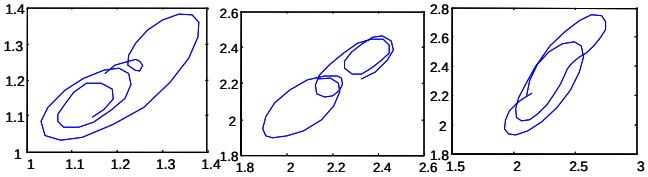

Fig. 4. (left to right) Trajectories obtained from a segment of the gas sensor response to discriminate NH_3 NO_2 and binary mixtures after apply the phase space.

5. Conclusions

In this paper we demonstrate how it is possible to optimize a multi-frequency signal to be used in the modulation of the operating temperature of an integrated gas sensor microarray using multi-level pseudo-random sequences. These frequencies selected are synthesized as multi-sinusoidal signals, and applied to modulate the working temperature of the microhotplate gas sensors.

References

[1] A.Vergara, E. Llobet, J. Brezmes, M. Stankova, P. Ivanov, X. Vilanova, I. Gràcia, C. Cané, X. Correig; Sensors, 2003. Proceedings of IEEE Volume 2, 22-24 Oct. 2003 Page(s):1255 - 1259 Vol.2

[2] K. Godfrey, Perturbation signals for system identification, Prentice Hall, UK, 1993.

[3] A. Vergara, E.Martinelli, E. Llobet, C. Di Natale, A. D'Amico, Boock of abstracts of ISOEN 2005 pp 40-42

Photosensitivity, Thermo-electrical properties and AC conductivity of Porous Silicon Devices.

F. Fonthal[1], T. Trifonov[1], A. Rodríguez[2], L.F. Marsal[1], J. Ferré-Borrull[1] and J. Pallarès[1]

[1]Departament d'Enginyeria Electrònica, Elèctrica i Automàtica; Universitat Rovira i Virgili, Avda. Països Catalans 26, Campus Sescelades 43007 Tarragona, Spain. Email: faruk.fonthal@urv.net
[2]Departament d'Enginyeria Electrònica, Universitat Politècnica de Catalunya, Barcelona, Spain

Abstract

In order to obtain electronic devices based on PS/p-Si structure, we present a study the AC conductivity, Thermo-electrical and Photosensitivity behavior of Porous Silicon (PS) layers prepared by electrochemical etching in two different <100> p-type silicon (p-Si) substrates. The beginning is obtaining good electrical contacts on porous layer; for this reason, several Au/PS/Au junctions were electrically characterized to understand the transport mechanisms in porous surface and the temperature dependent in the porous properties studied. An Au/PS/p-Si/Al structure was used for photosensitivity and spectral characterization. Finally, we obtained the AC conductivity in modulo and phase, also the resistance-temperature characteristic of PS/p-Si thermistor device and the photoresponse of the photodiode.

1. Introduction

Since the discovery that porous silicon (PS) may exhibit efficient visible photoluminescence (PL), there has been an extensive study of properties and different class for this material [1,2].

The light detecting property depends on the PS layer thickness and morphology. The minimization of the optical losses has been obtained by controlling the electrochemical etching for the formation of thin PS layers and by improvements in the photodetector fabrication [3,4].

An important aspect that should be addressed to obtain good electrical performance for these devices is the preparation of electrical contacts on the PS layer [5,6]. Therefore, it is important to study the AC electrical transport in PS/p-Si structure [7].

In this paper we present the resistance-temperature, AC conductivity and spectral range photoresponse characteristic of four PS devices.

2. Fabrication

P–type silicon wafers with <100> orientation and resistivities of 4-7 Ωcm and 7-9 Ωcm were used as starting material.

The PS layer was formed by electrochemical etching in ethanoic HF electrolyte (ethanol: HF 50%, 1:1 volume ratio).

Sample	Resistivity	Etching time
A	4-7 Ω cm	180 s
B	4-7 Ω cm	90 s
C	7-9 Ω cm	180 s
D	7-9 Ω cm	90 s

Table1. Characteristics of the fabricated samples.

The applied etching current density was 5 mA/cm^2. The anodization was performed for two different times - 90 s and 180 s. The etching conditions for the four samples studied are summarized in Table 1.

Finally, thin Au spots were evaporated on the porous silicon layer in order to obtain the electrical contact.

3. Results and discussion

Fig.1 show spectral characteristics of the Au/PS/p-Si/Al photodiode (sample D). Three regions in the spectral range were obtained. The first region from 338 nm to 380 nm, the second region from 400 nm to 470 nm and finally a regions in the near of IR from 900nm to 950 nm can be observed. The photocurrent linearly increases with the optical power of a white cold lamp (shown in the inset Fig.1). The measured sensitivities are 2.6 mA/W and 8.4 mA/W for samples with etching times of 90 s and 180 s, respectively.

We obtained a better responsivity and quantum efficiency of 2.35 A/W and 76.7%, respectively at 380 nm with 20V applied.

Fig. 2 show the temperature dependence of the resistance for the four Au/PS/Au thermistors fabricated together with data reported in other works [5]: thermally carbonized porous silicon TCPS, undoped polycrystalline SiC, RF-sputtered SiC, anodized p+-Si, a doped diamond. It was measured from 297 K to 393 K at 0 V. The calculated activation energies are 0.28 eV, 0.31 eV, 0.22 eV and 0.48 eV for samples A, B, C and D, respectively.

The high temperature coefficient (%K) obtained of the Au/PS/Au resistors at room temperature was 6.3%K for the sample fabricated using substrate of higher resistivity (7-9 Ωcm) and lower etching time (90 s) and is better that previously reported [5].

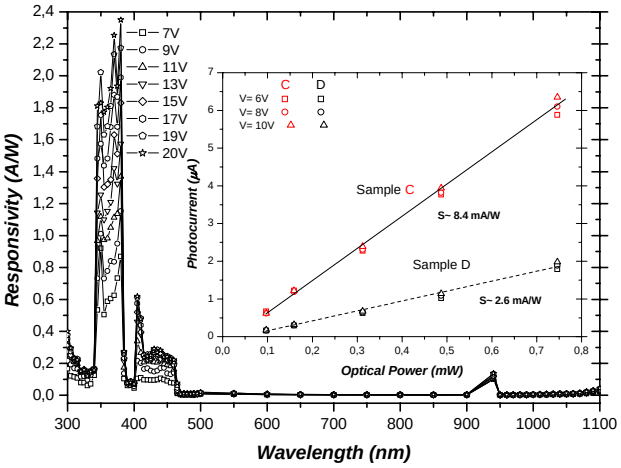

Fig.1. Spectral characteristic of Au/PS/p-Si/Al photodiode by different voltages applied. The photocurrent vs. optical power of both photodetectors measured at 6, 8 and 10V is shown in the inset.

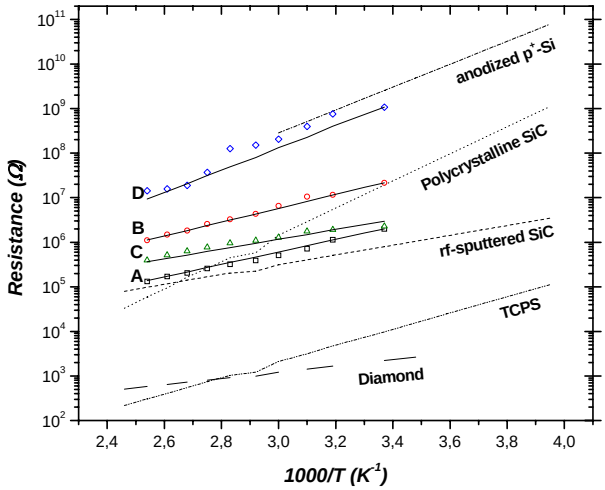

Fig.2. Resistance-temperature dependence for the four thermistors studied, at 0 V. Thermistor equation fitted (line) to the measured values (symbol) at room temperature.

Fig. 3 shows the conductivity and capacitance characteristics for the four Au/PS/Au resistors fabricated. The theoretically behavior of the impedance *Z* of the equivalent circuit in the samples studied of Fig.4 is:

$$Z(\omega) = R_s + \frac{R_{sh}}{(iR_{sh}\omega C + 1)} \qquad (2)$$

The lowers conductance and capacitance values were obtained for the sample fabricated using lower etching time (90 s) and for the sample fabricated with higher resistivity (7-9 Ωcm) we obtained the highest resistance of the resistors fabricated.

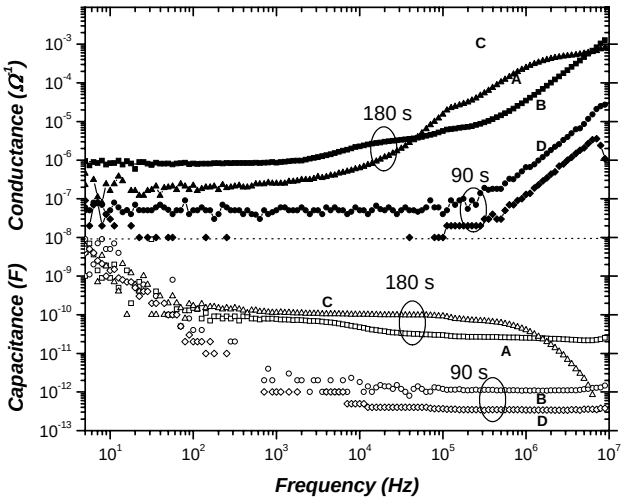

Fig.3. AC Conductivity and Capacitance characteristic for the four samples fabricated, at 0 V.

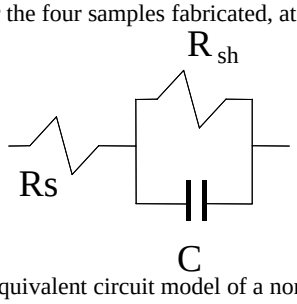

Fig.4. Equivalent circuit model of a nonideal resistor.

4. Conclusions

The fabrication, Thermo-electrical DC and AC, the optical characterization of PS/p-Si devices based on porous silicon has been reported.

A responsivity of 2.35 A/W at 380-nm with 20V applied in the more sensitivity region, have been obtained.

The devices showed an ohmic contact. It was found that the measured resistance depends more on the etching time than on the wafer resistivity. The highest resistance value has been obtained for the sample fabricated using substrate of higher resistivity (7-9 Ωcm) and lower etching time (90 s).

An equivalent circuit has been determined for the AC electrical behaviour of the resistance. Lowers conductance and capacitance values have been obtained for the sample fabricated using lower etching time (90 s).

References

[1] L.T. Canham, *Appl. Phys. Lett.*, 57 (1990), pp. 1046-1048.
[2] V.Parkhutik, *Solid-State Elect*, 43 (1999), pp. 1121-1141.
[3] A.M Rossi, H.G. Bohn, *Phys. Stat. Sol. A*, 202(8) (2005), pp. 1644-1647.
[4] F.Fonthal, T. Trifonov, A. Rodríguez, L.F. Marsal, J. Ferré-Borrull, J. Pallarès, EurosensorsXIX, (2005), (accepted).
[5] J. Salonen, M. Björkqvist, J. Paski, *Sensors and Actuators A*, 116 (2004), pp. 438-441.
[6] D. Yarkin, L. Balagurov, S. Bayliss, I Zvyagin, *Semicod. Sci. Techno*, 19 (2004), pp. 100-105.
[7] A. Straub, R. Gebs, H. Habenicht, S. Trunk, R. A. Bardos, A. B. Sproul, A.G. Aberlea, *J. Appl. Phys.* 97 (2005), pp. 083703-083703-8.

Design and fabrication of grating-waveguides for biosensing applications.

N. Darwish, M. Moreno, F. Muñoz*, R. Mas*, J. Samitier

Departament d'Electrònica, Facultat de Física, Universitat de Barcelona
C/ Marti i Franques 1, 08028, Barcelona
* Centro Nacional de Microelectrónica, Campus UAB, 08193, Bellaterra
ndarwish@el,ub.es, moreno@el.ub.es, pxm@cnm.es roser.mas.@cnm.es, samitier@el.ub.es

Abstract

In this document we will describe the design of some grating coupler systems and the experimental results for them at the laboratory. These elements have been designed to act as the transducer parts of optical biosensors [1].

Biosensors based on grating couplers.

In figure 1 we can see two types of grating couplers. Subfigure (I) represents a grating etched on the waveguide surface, in the interface between it and an external medium. The light coupling in the guide, due to the presence of a grating, in the thin layer approximation [2] is governed by next expression:

$$n_{eff} = n_{ext} \sin\alpha_l + l\frac{\lambda}{\Lambda} \qquad (1)$$

where n_{eff} is the effective index for the guided mode, λ is the wavelength, Λ is the grating period, and α is the coupling angle. The diffractive order is represented by *l*. This last parameter has a strong effect on the sensitivity. Once specified a waveguide, the whole set of coupling angles are determined by the number of modes the guide support, and the diffractive orders the system allows to couple. Considering that our waveguides are monomode, only the second parameter is important, and the angle we see depends only on what diffractive order we are observing. Subfigure (II) represents a system where the light is always coupled at the same angles, avoiding the need to use mobile pieces.

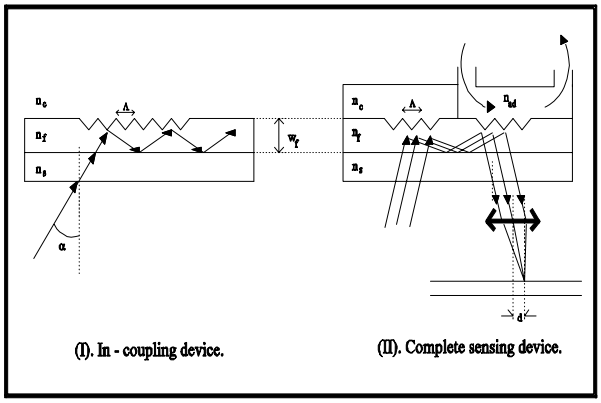

Fig.1. Two grating coupler configurations. We have n_s, n_f, n_c, respectively, the refractive indexes of the substrate, the film layer and the cover medium.

After a while travelling through the guide, the light finds other grating, exposed to a different medium, and is coupled out in a set of angles that depends on its effective refractive index. Using a model of the guide, we can obtain its parameters. In this document we only discuss the analysis of the cover refractive index. We also can analyze the thickness of some adlayer that varies with the concentration of any substance we can immobilize, like for the inmuno-sensing systems [3, 4].

Some results

At first, we wanted to design the most sensitive waveguides. In figure 2 it's shown the sensitivity of a silicon nitride waveguide to changes in the cover medium refractive index, as a function of its thickness, for water as the cover medium, and at a wavelength of 633nm. In figure 3, using different gratings, we analyze the angular sensitivity for the same system. The guides have been simulated using the method described in [5].

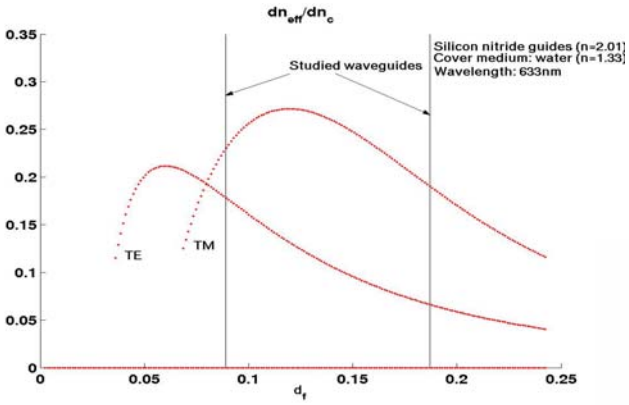

Fig.2. Sensitivity of the effective refractive index to the cover index changes, in front of the guide thickness. The wavelength is 633nm.

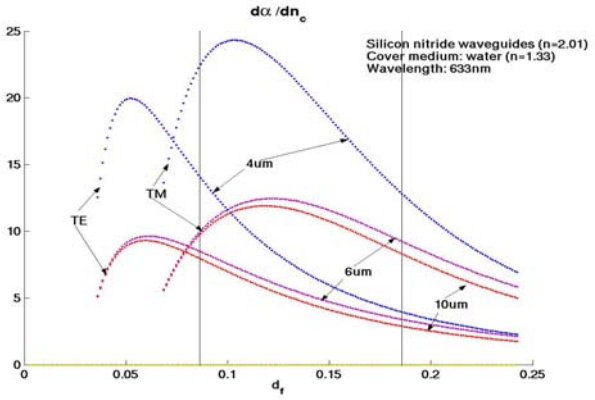

Fig.3. Angular sensitivity for the same conditions, using gratings of Λ=4, 6 and 10 microns of period.

Considering these results, we decided to fabricate waveguides of 90 and 180nm (figure 4). These values correspond to monomode waveguides for both TE and TM modes. The grating periods of 4, 6 and 10 microns are inside our technology restrictions. Thicknesses and grating periods are different enough to have a nice set of different systems to compare. Finally, we made two grating etching depths of 10 and 20nm.

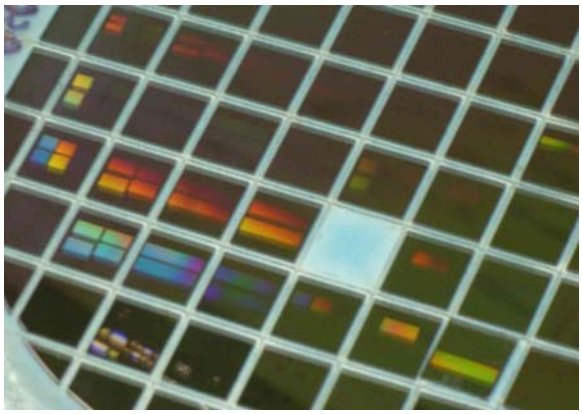

Fig.4 One of the wafers. It can be seen the configurations of fig.1, showing one or two gratings. The etching depth of the gratings are 10nm and 20nm.

We measured the coupling angles in the optical bench using a custom fluidic cell, for air and water as two different cover media, and for TE and TM modes. In figure 5 it's shown the theoretical curve for air and the corresponding experimental values. All the angles measured are in a 10' precision limit around the theoretical curve.

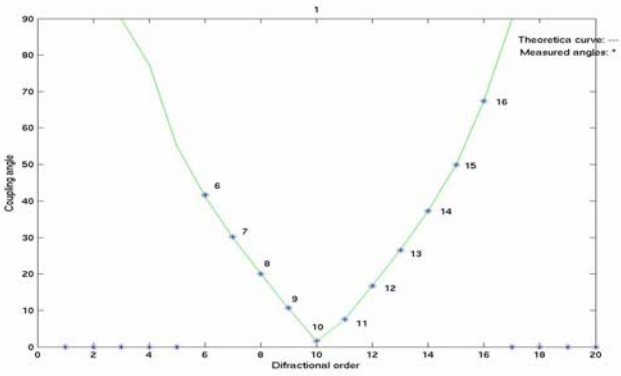

Fig.5. Comparison between theoretical and practical results for TM mode and water as the cover medium. Wavelength: 633nm, waveguide thickness: 180nm, grating period: 4 microns, etching depth: 20nm.

Conclusions

We have shown here that it is possible to make a sensing system able to detect variations of 0.001 in the cover refractive index, using gratings of 4 microns of period. The gratings used in previous works [3] have periods under one micron. The advantage of lower period gratings is a greater coupling efficiency, allowing less sensitive detectors to find the coupling angles, and the advantage of greater period guides is that permit us to use cheaper technologies. In our scheme, the possibility to see various diffractive orders permit us to see various coupling angles simultaneously. The redundant angular information can be considered as an advantage, because we can adjust it to cancel possible erroneous measures.

References

[1] K. Tiefenthaler and W. Lukosz, "Sensitivity of grating couplers as integrated-optical chemical sensors", J. Opt. Soc. Am. B, Vol. 6, No 2, Feb. 1989.

[2] R.E.Kunz, J. Dübendorfer & R. H. Morf, "Finite grating depth effects for integrated optical sensors with high sensitivity", Biosensors & Bioelectronics, Vol. 11, No 6/7 (1996), pp 653-667.

[3] W. Lukosz, "Integrated optical chemical and direct biochemical sensors", Sensors and Actuators B, 29 (1995) pp 37-50.

[4] R.E. Kunz, "Miniature integrated optical modules for chemical and biochemical sensing", Sensors and Actuators B, 38-39 (1997) 13-28.

[5] Ajoy K. Ghattak, K. Thyagarajan, M. R. Shenoy, "Numerical analysis of planar optical waveguides using matrix approach", Journal of lightwave technology, Vol. LT-5, No 5, May 1987.

A Nonlinear FDTD Approach for Dispersion Characteristic Calculation

I. S. Maksymov, L. F. Marsal and J. Pallarès

Departament d'Enginyeria Electrònica, Elèctrica i Automàtica, Universitat Rovira i Virgili, Campus Sescelades, Avda. Països Catalans 26, 43007 Tarragona, Spain
Tel.: +34 977 559 625, Fax: +34 977 559 605, E-mail: lluis.marsal@urv.net

We present an approach for analyzing dispersion characteristics of nonlinear photonic crystal waveguides. This approach combines the nonlinear finite-difference time-domain method, based on the numerical simulation of oscillating dipole radiation [1-3], with the super cell strategy and the periodic boundary conditions. The source code based on the approach presented makes it possible to calculate the dispersion characteristics of Kerr-like nonlinear photonic crystals waveguides made by removing some scatterers.

Figure 1 shows an example of the geometry that can be considered and the corresponding result. The structure considered is a coupled cavity waveguide based on evanescent coupling between modes of neighbouring resonators. The properties of the material of the rods are chosen to be equal to those of AlGaAs [4].

In order to carry out the calculation, the super cell (figure 1 (a)) is divided into 60x140 cells. The dispersion curves calculated with our code are shown in figure 1 (b). The solid line corresponds to the linear dispersion characteristic whereas the dot and dash lines correspond to the nonlinear dispersion characteristics. The incident intensities are 9.5 GW/cm^2 and 16 GW/cm^2. These values are calculated at $\frac{ka}{2\pi} = 0$. As we can see, for the nonlinear regimes there are red-shifts of the dispersion curves with regard to the linear regime.

In conclusion, a numerical tool based on this technique can be used to design various components for integrated optical circuits.

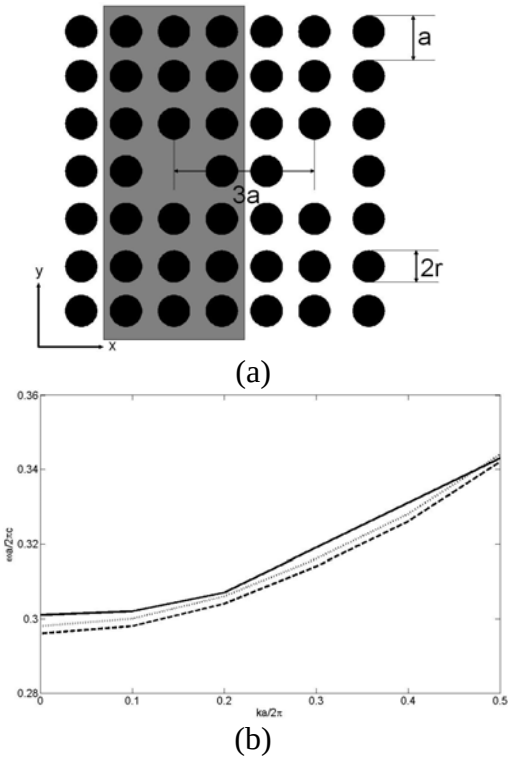

Fig. 1. (a) Geometry of the coupled-cavity nonlinear photonic crystal. Gray region denotes the super cell used for the calculation of the dispersion characteristic. (b) The dispersion characteristics calculated for the linear (solid line) and nonlinear (dash line) regimes.

References

[1] I. S. Maksymov, L. F. Marsal and J. Pallares. *Opt. Commun.* **248** 469, 2005.
[2] I. S. Maksymov, L. F. Marsal and J. Pallares. *Proceedings of the 13th International Workshop on Optical Waveguide Theory and Numerical Modelling*, Grenoble, France, 8-9 April 2005.
[3] I. S. Maksymov, L. F. Marsal and J. Pallares. *Proceedings of the 6th Symposium on Photonic and Electromagnetic Crystal Structures*, Crete, Greece, 19-24 June 2005.
[4] J. S. Aitchison, D. C. Hutchings, J. U. Kang, G. I. Stegeman and A. Villeneuve. *IEEE J. Quantum Electron.* **33** 341, 1997.